

Calculation of Peridotite Partial Melting from Thermodynamic Models of Minerals and Melts, IV. Adiabatic Decompression and the Composition and Mean Properties of Mid-ocean Ridge Basalts

P. D. ASIMOW^{1*}, M. M. HIRSCHMANN² AND E. M. STOLPER¹

¹DIVISION OF GEOLOGICAL AND PLANETARY SCIENCES, CALIFORNIA INSTITUTE OF TECHNOLOGY M/C 170-25, PASADENA, CA 91125, USA

²DEPARTMENT OF GEOLOGY AND GEOPHYSICS, UNIVERSITY OF MINNESOTA, 310 PILLSBURY DRIVE SE, MINNEAPOLIS, MN 55455-0219, USA

RECEIVED JANUARY 25, 2000; REVISED TYPESCRIPT ACCEPTED AUGUST 16, 2000

Composition, mean pressure, mean melt fraction, and crustal thickness of model mid-ocean ridge basalts (MORBs) are calculated using MELTS. Polybaric, isentropic batch and fractional melts from ranges in source composition, potential temperature, and final melting pressure are integrated to represent idealized passive and active flow regimes. These MELTS-derived polybaric models are compared with other parameterizations; the results differ both in melt compositions, notably at small melt fractions, and in the solidus curve and melt productivity, as a result of the self-consistent energy balance in MELTS. MELTS predicts a maximum mean melt fraction (~ 0.08) and a limit to crustal thickness (≤ 15 km) for passive flow. For melting to the base of the crust, MELTS requires an $\sim 200^\circ\text{C}$ global potential temperature range to explain the range of oceanic crustal thickness; conversely, a global range of 60°C implies conductive cooling to ~ 50 km. Low near-solidus productivity means that any given crustal thickness requires higher initial pressure in MELTS than in other models. MELTS cannot at present be used to model details of MORB chemistry because of errors in the calibration, particularly Na partitioning. Source heterogeneity cannot explain either global or local Na–Fe systematics or the FeO–K₂O/TiO₂ correlation but can confound any extent of melting signal in CaO/Al₂O₃.

KEY WORDS: mantle melting; mid-ocean ridge basalt; peridotite composition; primary aggregate melt; thermodynamic calculations

INTRODUCTION

Comparison of observed basalt compositions with the predictions of polybaric mantle melting models places important restrictions on melting processes in the mantle beneath mid-ocean ridges (Klein & Langmuir, 1987; McKenzie & Bickle, 1988; Niu & Batiza, 1991, 1993; Kinzler & Grove, 1992b; Langmuir *et al.*, 1992; Iwamori *et al.*, 1995; Kinzler, 1997). It is now well accepted that mid-ocean ridge basalts (MORBs) represent mixtures of melts produced over a range of depths and that these melts separate from their sources at low melt fraction (McKenzie, 1984; von Bagen & Waff, 1986; Johnson *et al.*, 1990; Langmuir *et al.*, 1992). However, significant uncertainties remain regarding the depth of initial melting (related both to the range of mantle potential temperature and to the influence of minor incompatible components on the solidus), the depth of final melting (and hence the importance of spreading rate), the style of melt transport (e.g. the relative importance of fractional fusion vs equilibrium porous flow), and the effects of chemical heterogeneities in mantle sources. These uncertainties remain for a number of reasons (among them disagreements over the selection of data, the appropriate scale for averaging, and corrections for fractionation), but a key

*Corresponding author. Telephone: 626-395-4133. Fax: 626-568-0935. E-mail: asimow@gps.caltech.edu

factor is that mantle melting algorithms have not been sufficiently accurate to evaluate quantitatively the consequences of competing hypotheses or to incorporate the complexities of the physics of melting and melt transport.

Langmuir *et al.* (1992) identified three functions that must be combined to create a forward model capable of quantitative prediction of the magmatic output of the mantle beneath mid-ocean ridges: a chemistry function, a melting function, and a mixing function. The chemistry function specifies the liquid composition as a function of pressure (P), temperature (T) (or, alternatively, of P and extent of melting, F), and source composition. The melting function specifies F for a single parcel of source as a function of P and T and the path (usually approximated as adiabatic) through (F, P, T) space. The mixing function is a representation of the 2D (or, in principle, 3D) form of the melting regime and specifies how the individual increments of liquid generated continuously over a range of depths and distances from the ridge axis are to be weighted to create an aggregate primary melt. These three functions are often constructed independently, but in fact the chemistry and melting functions are intimately dependent on one another, as both must satisfy mass and energy balance and both are controlled by the same thermodynamics of solid–liquid equilibrium. Furthermore, the possibility of reaction between melt and matrix during melt migration means that the mixing problem cannot be separated from the chemistry and melting functions (Spiegelman, 1996; Kelemen *et al.*, 1997). There are several published chemistry, melting, and mixing functions based on parameterization of experimental peridotite melting data (Klein & Langmuir, 1987; McKenzie & Bickle, 1988; Niu & Batiza, 1991; Kinzler & Grove, 1992a, 1992b; Langmuir *et al.*, 1992; Kinzler, 1997).

Over the past several years, we and our colleagues have been utilizing the MELTS algorithm (Ghiorso, 1994; Ghiorso & Sack, 1995) as a tool for trying to understand aspects of experiments on peridotite melting (Baker *et al.*, 1995; Hirschmann *et al.*, 1998b, 1999a, 1999b) and as a basis for forward models of polybaric mantle melting and of coupled melting and two-phase flow in upwelling mantle (Asimow, 1997; Asimow *et al.*, 1997; Asimow & Stolper, 1999). The forward models of polybaric melting we utilize differ from other algorithms in that MELTS provides a self-consistent thermodynamic approach to the chemistry and melting functions. Although we must emphasize that MELTS is not sufficiently accurate to address in detail some key questions raised by the observed compositional variations of MORB magmas, it is nevertheless the first approach that allows a full and self-consistent integration of the thermodynamics and phase equilibria of partially molten peridotitic systems. For this reason, it is ideal for examining important issues such as the interplays between the depth-dependent

productivity of upwelling mantle and the average composition and pressure of melting and between source heterogeneity and productivity.

In this paper, we present a set of polybaric calculations of mantle melting using MELTS. These calculations build on related isobaric calculations (Hirschmann *et al.*, 1998b, 1999a, 1999b) and on polybaric, isentropic calculations (Asimow *et al.*, 1995, 1997) and are used to illustrate both the potential and current limitations of the method. All calculations herein use the calibration of MELTS documented by Ghiorso & Sack (1995); this is the calibration underlying the widely distributed MELTS 2.0 package, and although we have modified the implementation for convenience, we have not altered the model in any way. This paper does not include results from newer calibrations such as pMELTS (Ghiorso & Hirschmann, in preparation). In general, MELTS predicts isobaric trends of composition vs melt fraction that are similar to those observed in experiments, but the calculated trends are frequently offset in T and in the concentrations of certain oxides. For example, at 1.0 GPa the best match in F between MELTS and experiments is obtained with an offset of 80°C in T and the resulting model liquids are ~4% (absolute) too low in SiO₂ and 2% too high in MgO (Baker *et al.*, 1995). Comparison with experiments has also shown that MELTS yields too low a peridotite–liquid partition coefficient for Na (Hirschmann *et al.*, 1998b). Given these inaccuracies in the current calibration of MELTS, we focus on using it as a tool for studying trends in relationships among variables rather than to predict the actual values of specific parameters. Accurate quantitative modeling of absolute values of compositional variables and phase proportions as functions of pressure, potential temperature, etc. is certainly possible with the approach we use here, but it will depend on improving or customizing the calibration.

The mixing function depends on geodynamic considerations such as the form of the solid flow field and melt extraction pathways. Our focus in this paper is on insights from thermodynamic modeling of melt composition and melting, so we limit our treatment to the simplest end-member mixing functions associated with either perfect active or perfect passive flow [we use standard definitions of mixing functions and mean properties from Plank *et al.* (1995); see details below in the section ‘Mean properties of melting regimes’]. Although all the calculations presented here use one of these two simple mixing functions, we will conclude in many places that neither function is adequate and that progress in modeling of ridges will depend on using physically based mixing functions.

One of the recurring issues in our modeling of melting at ridges will be an examination of the consequences of two competing views of the principal controls on variation

of average magma compositions among ridge segments. Klein & Langmuir (1987) and others (McKenzie & Bickle, 1988; Klein & Langmuir, 1989; Langmuir *et al.*, 1992; Plank & Langmuir, 1992) considered that, except perhaps at very slow-spreading rates, melting continues to a shallow depth, perhaps the base of the crust, at all ridge segments. Variations in average MORB composition on the world-wide ridge system, correlated with ridge topography and seismic velocity in the underlying mantle (Klein & Langmuir, 1987; Humler *et al.*, 1993; Zhang *et al.*, 1994), were then attributed primarily to variations in the potential temperature (T_p) of the upwelling mantle (a range of 200–250°C, Klein & Langmuir, 1987; or 300°C, McKenzie & Bickle, 1988), which controls the intersection of the adiabat with the solidus and thus the initial pressure of melting (P_o). We will refer in this work to this model of global variations as ‘variable- P_o ’ systematics. Shen & Forsyth (1995), on the other hand, attributed the variability in the compositions of MORBs primarily to the effectiveness of cooling from the surface and hence to the final pressure of melting (P_f). The total variation in potential temperature among non-hotspot-affected ridges was then estimated to be $\sim 60^\circ\text{C}$ (Shen & Forsyth, 1995). A consistent model based on this second view generally includes a significant role for heterogeneous source compositions (Niu & Batiza, 1991; Shen & Forsyth, 1995) and implies a correlation of extent of melting with spreading rate (Niu & Batiza, 1993; Niu & Hékinian, 1997*a*, 1997*b*). We refer to this model of global variations as ‘variable- P_f ’ systematics.

Evaluation of variability and correlations among compositions of MORB samples requires correcting for the effects of low-pressure fractionation so as to isolate the effects of magma generation processes in the mantle (Klein & Langmuir, 1987). In this work we restrict our attention mostly to model primary liquid compositions based on MELTS and compare them with other workers’ model primary aggregate liquids; i.e. we generally do not attempt to fractionate these model liquids to compare them with actual MORB data or with MORB data corrected for fractionation (i.e., we discuss mostly Na_2O and FeO^* rather than Na_8 or Fe_8 , the equivalent values corrected for low-pressure fractionation to 8% MgO; Klein & Langmuir, 1987). We take this approach for several reasons. First, the 8% MgO standard obscures real variations in the MgO content of primary aggregate liquids; in particular, calculations herein are extended to the low potential temperature extreme where the primary liquid may have <8% MgO, which would require an artificial back-fractionation step. Second, the correction is difficult to perform quantitatively in most cases. The low SiO_2 and high Na_2O in liquids predicted by MELTS (Hirschmann *et al.*, 1999*b*) results in primary aggregate liquids that are nepheline normative and do not follow tholeiitic fractionation paths, whether fractionated using

MELTS or any other fractionation model. The model of Weaver & Langmuir (1990) is not calibrated on alkalic liquids, but yields a tholeiitic fractionation path for MELTS primary aggregate liquids that we use here with some caution. Moreover, the Langmuir *et al.* (1992) model does not predict CaO or Al_2O_3 in primary liquids, but these are essential components in determinations of pyroxene and plagioclase stability and the effects of these phases on liquid lines of descent, so comparison between our model primary liquids and those of Langmuir *et al.* (1992) is best performed without first fractionating them to 8% MgO. Nevertheless, much can be learned from examination of model primary liquids, particularly as the effects of fractionation are relatively minor for several of the elements of interest.

Recent efforts to interpret MORB compositions in terms of magma generation processes have, in addition to corrections for fractionation, distinguished variability among individual MORB samples within a region from variability on a global scale among regional averages of samples (Brodholt & Batiza, 1989; Klein & Langmuir, 1989). Correlations among regional averages are generally termed ‘global trends’ whereas correlations in variations among individual samples from a segment are termed ‘local trends’. Forward models of melting of the sort presented in this paper can be used to examine the possible spectrum of local variability by examining all the incremental melt compositions and partial mixtures among them that can be produced from a model melting regime (although the large range of partial mixing models that can be devised makes it difficult to specify *a priori* the particular local trend that will result from a given model melting regime).

In this paper, we begin by introducing phase diagrams in pressure–temperature and pressure–entropy space that set up the framework for all MELTS predictions of polybaric melting by showing where each phase assemblage is predicted to be stable and the contours of equal melt fraction above the solidus [the importance of which was discussed by Asimow *et al.* (1997)]. The coupling between the chemistry and melting functions predicted by MELTS is then illustrated using the SiO_2 vs melt fraction (F) plot of Klein & Langmuir (1987). A brief discussion of the differences between isentropic batch melting and incrementally isentropic fractional melting (Asimow *et al.*, 1995, 1997) introduces comparisons between mean properties of the melting regime (i.e. mean pressure, mean extent of melting, and crustal thickness) as functions of the initial and final pressures of melting. This is followed by predictions of correlations of these mean properties with compositional trends in primary aggregate liquids, particularly Na_2O and FeO^* . Finally, we consider the effects of variable source composition on primary aggregate liquid compositions,

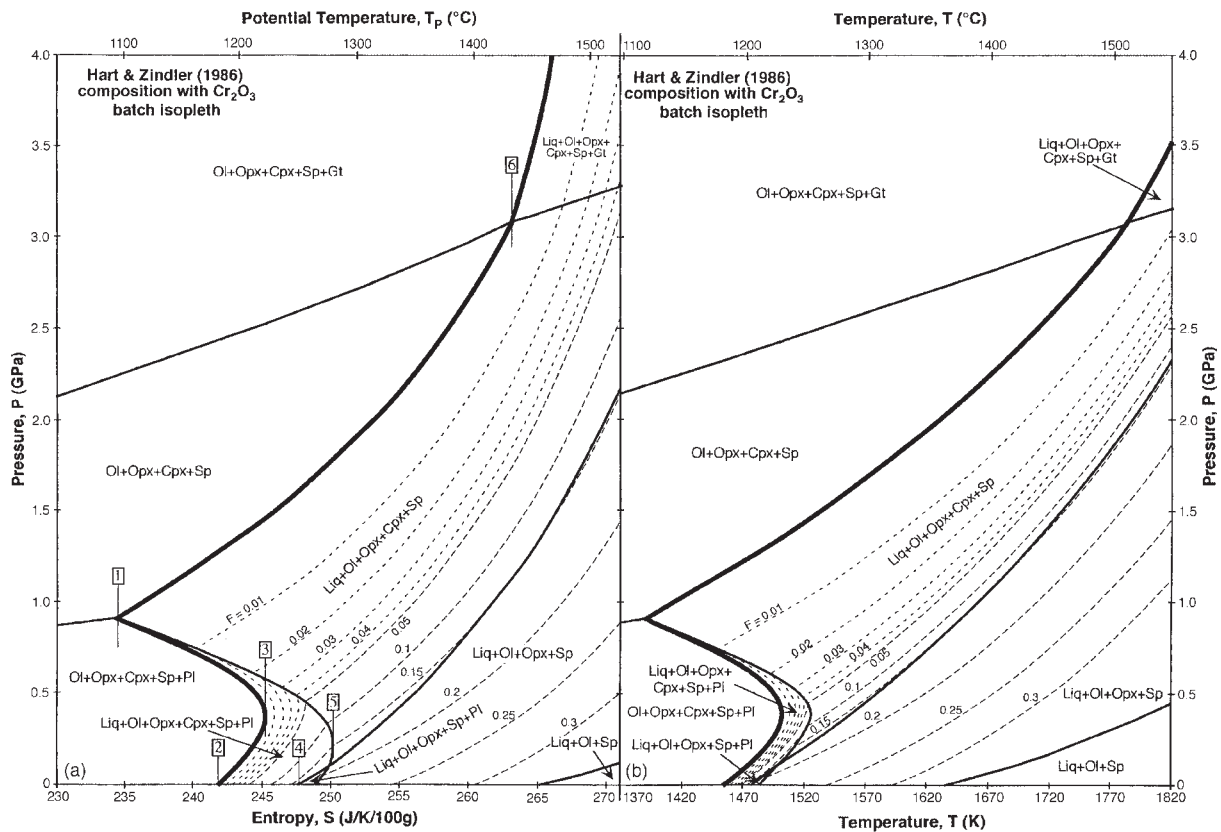


Fig. 1. (a) and (b).

extending the discussion of Hirschmann *et al.* (1999b), which dealt only with calculations of isobaric melting.

ISENTROPIC BATCH MELTING

Figure 1 shows maps of the stable phase assemblages for a model primitive mantle composition (Hart & Zindler, 1986), with and without Cr_2O_3 . The axes in Fig. 1a and c are P and specific entropy (S), or equivalently P and potential temperature [T_p , the calculated temperature of the metastable solid assemblage at 1 bar with the given total S , allowing all solid reactions to reach equilibrium; see McKenzie & Bickle (1988)]. ‘Ordinary’ temperature (T) is plotted vs P in Fig. 1b and d for reference, but P and S are the appropriate independent variables for reversible adiabatic (i.e. isentropic) melting (Verhoogen, 1965; McKenzie, 1984; Asimow *et al.*, 1995, 1997). Any vertical line in a P - S diagram corresponds to a batch isentropic path. Contours of constant extent of melting by mass, F , are plotted in the supersolidus region of each map. The isentropic productivity of batch melting at any point is inversely proportional to the spacing of these contours as they intersect a vertical path. Hence, these diagrams show all possible isentropic batch melting paths

for this source composition and the range of mantle potential temperatures likely to be seen by modern mid-ocean ridges. Although absolute temperatures at elevated pressure in the following discussion are subject to the errors noted by Baker *et al.* (1995) and Hirschmann *et al.* (1998b) and are likely to be $\sim 80^{\circ}\text{C}$ hotter than the correct temperatures, potential temperature is defined at atmospheric pressure where MELTS is much more accurate. T_p values obtained from MELTS can be compared directly with T_p estimates from other models, with an uncertainty of perhaps 20°C .

For $T_p < 1100$ – 1120°C (boxed 1 in Fig. 1a and c), melt does not form at any pressure. Although this may be an artifact of MELTS and needs further investigation (see below), it is interesting that this minimum temperature, roughly the same for the Cr-bearing and Cr-absent cases, is not determined by the solidus temperature at 1 bar or at the base of the crust but rather by the location of the six-phase point olivine + orthopyroxene + clinopyroxene (cpx) + spinel + plagioclase + liquid; i.e. the point of the cusp on the solidus. This is the point on the MELTS-calculated solidus with the lowest specific entropy, and so it defines the lowest mantle potential temperature at which the adiabat intersects the solidus.

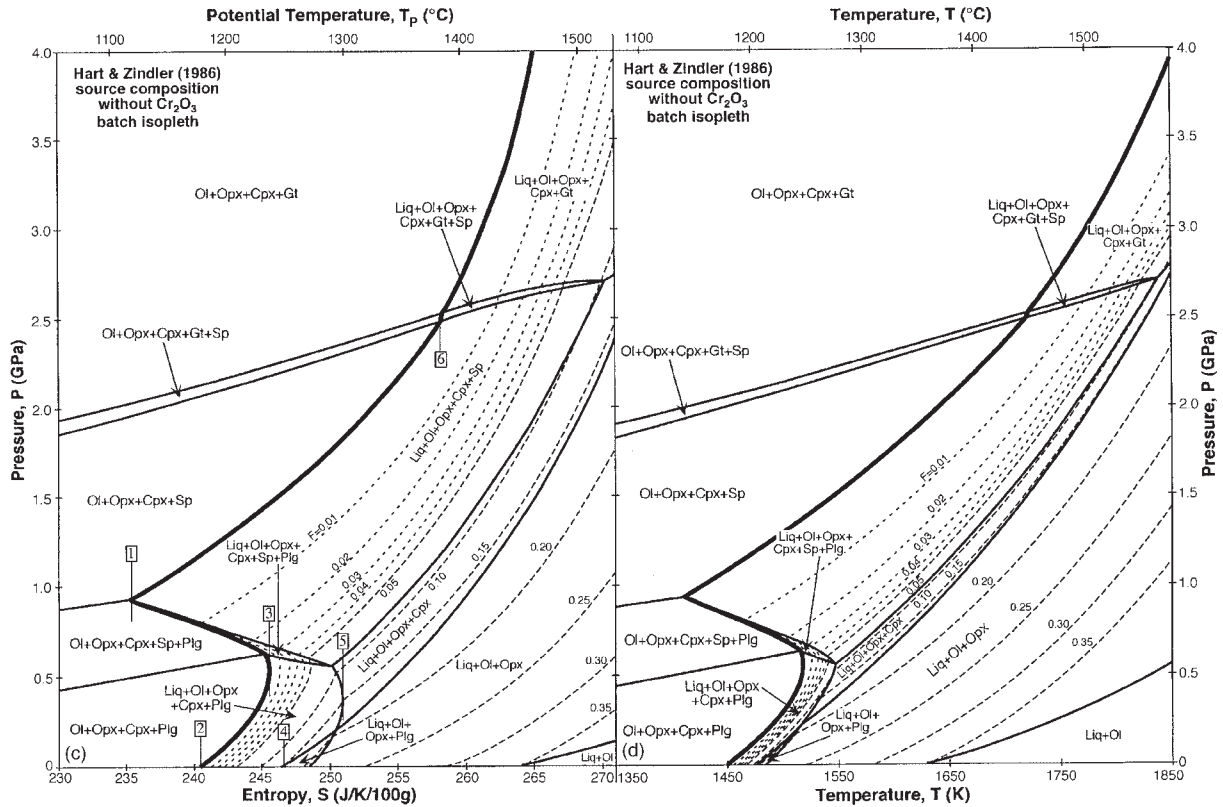


Fig. 1. (a)–(d) Maps of the stable phase assemblages predicted by MELTS for constant bulk compositions. In the region where liquid is present, the mass fraction of liquid (F) is contoured. Contours at 1% intervals for F up to 0.04 are shown dotted. Contours at 5% intervals for $F \geq 0.05$ are shown dashed. (a) and (b) use the primitive upper-mantle composition of Hart & Zindler (1986); (c) and (d) use a Cr-free equivalent. The axes in (a) and (c) are pressure (P) on the vertical axis and specific entropy (S) and potential temperature (T_p) on the bottom and top horizontal axes. A vertical line on these diagrams is an isentropic batch melting path. In (b) and (d) the horizontal axis is temperature (T). Ol, olivine; Opx, orthopyroxene; Cpx, clinopyroxene; Sp, spinel; Gt, garnet; Pl, plagioclase; Liq, liquid. Numbers in boxes refer to special points of interest mentioned in the text.

Melting paths with $\sim 1110^\circ\text{C} < T_p < 1225^\circ\text{C}$ (boxed 1–3 in Fig. 1a and c) freeze completely as a result of the spinel–plagioclase transition (Asimow *et al.*, 1995). These paths achieve peak melt fractions of $F \leq 0.025$ in the spinel peridotite field. Those paths hotter than $T_p \sim 1175^\circ\text{C}$ (boxed 2 in Fig. 1a and c) would begin melting again in the plagioclase stability field if isentropic decompression continued all the way to 1 bar. All paths up to $T_p \sim 1275^\circ\text{C}$ with Cr_2O_3 (boxed 5 in Fig. 1c) have plagioclase in the residue for at least a small interval. $T_p \sim 1250^\circ\text{C}$ (boxed 4 in Fig. 1a and c) is the minimum for exhaustion of cpx from the residue. For the Cr-bearing case, $T_p > \sim 1425^\circ\text{C}$ (boxed 6 in Fig. 1a) is required for melting to begin in the garnet field; for the Cr-absent case garnet is calculated to be present on the solidus for $T_p > \sim 1380^\circ\text{C}$ (boxed 6 in Fig. 1c).

The shape of the MELTS-calculated solidus has two unusual features: the negative slope of the solidus at

pressures just below that of the spinel–plagioclase transition and the substantial curvature of the solidus in the spinel and garnet stability fields, which leads to a maximum in T_p on the solidus near 6.5 GPa (not shown in Fig. 1). Although simple considerations of phase diagram topology dictate that there must be a cusp on the solidus at the appearance of plagioclase (Presnall *et al.*, 1979), the calculated result that there is actually a temperature drop with increasing pressure approaching the cusp is surprising. This predicted shape reflects primarily the solidus-lowering capacity of Na, which is enhanced in the spinel peridotite field relative to the plagioclase peridotite field by the greater incompatibility of Na in assemblages with less plagioclase. In this sense, the region of negative slope on the solidus is similar to that observed for amphibolite (Wyllie & Wolf, 1993) or amphibole-bearing peridotite (e.g. Green, 1973) where the breakdown of amphibole near 2.0–2.5 GPa converts water from a

relatively compatible to an incompatible component. It is possible that the prediction of a minimum temperature at the cusp is an artifact of MELTS, as MELTS overestimates the incompatibility of Na in the spinel peridotite field (Hirschmann *et al.*, 1998b), and, indeed, this shape has not been observed in experimental determinations of peridotite solidi. However, examination of the melt fraction contours in Fig. 1 shows that the shape as determined by experiment would be extremely sensitive to the minimum melt fraction required to identify melting in an experiment. For example, at $F = 0.01$, the temperature drop at the cusp is predicted to be only half as big as that on the solidus itself, and by $F = 0.05$, there is no temperature drop or negatively sloped region at all. Thus, experimental determinations of peridotite solidi, none of which have yet systematically explored such low melt fractions, are unlikely to have detected such behavior even if it does occur, as it is predicted to be confined to such small melt fractions.

Although MELTS as currently formulated was not intended to be used at pressures beyond ~ 2 GPa (Ghiorso & Sack, 1995), the phase relations implicit in MELTS require that calculated melting begins deeper than this to model ridge segments with more than ~ 4 km of crust. Although we have little confidence in specific predictions of the model (e.g. liquid compositions) above ~ 3 GPa, the position and shape of the solidus are critical factors in forward modeling amounts of melt production and crustal thickness on a given isentropic path. The solidus of the KLB-1 peridotite composition (for which the most data are available at high P) predicted by MELTS is compared in Fig. 2 with experimental brackets. This figure shows that the MELTS-calculated solidus for KLB-1 is similar (i.e. within 100°C) to all experimental brackets up to at least 8 GPa (Takahashi, 1986; Takahashi *et al.*, 1993; Zhang & Herzberg, 1994). The MELTS solidus is also everywhere within 75°C of the solidus that McKenzie & Bickle (1988) fitted to peridotite solidus data (with only KLB-1 points above 4 GPa), but the MELTS solidus is more strongly curved and has a lower slope at very high pressure. MELTS tends to exaggerate the incompatibility of Na near the solidus, leading to too large a 'freezing point depression' (Hirschmann *et al.*, 1998b), whereas at higher melt fractions it errs in the opposite direction by $\sim 80^\circ\text{C}$ at 1 GPa (Baker *et al.*, 1995), so the excellent correspondence between the calculated and measured solidus in Fig. 2 could be misleading. None the less, the similarity in the overall curvatures of the model and experimental determinations of the solidus in P - T space is useful in the context of forward models of melt production as a function of potential temperature. Although the magnitude of the calculated curvature may be exaggerated by errors in MELTS that grow worse with increasing pressure, it is particularly important that the MELTS calculations and experiments both display the

flattening of the solidus expected as a result of the greater compressibility of liquid silicate components compared with minerals (Walker *et al.*, 1988). Figure 2 also shows that the linear solidus with a slope of 130 K/GPa assumed by Langmuir *et al.* (1992) corresponds well to the more complex solidus calculated by MELTS and to the experimental determinations of the solidus up to a pressure of ~ 5 GPa, beyond which it increasingly diverges from both the data and the MELTS calculation.

As emphasized by Asimow *et al.* (1997), phase relations are typically more useful for understanding decompression melting when portrayed in S - P (or equivalently T_p - P) space than when portrayed in P - T space. There are no experimental measurements of entropy or potential temperature, of course, but when recast in these terms, mantle melting is more easily visualized, and insights can be obtained that would be difficult using P and T as the independent variables. In the case of MELTS calculations on the Hart & Zindler composition, with or without Cr, the solidus is actually predicted to have a vertical tangent at 6.4 GPa (off the tops of Fig. 1a-d) and ~ 2000 K ($T_p \sim 1500^\circ\text{C}$). If such a maximum on the solidus in S - P space exists, it would have some curious consequences, including progressive freezing of parcels of mantle as they decompress from higher pressures. Determination of whether such a maximum in entropy along the solidus actually exists for upper-mantle materials must await improved thermodynamic data on solids and liquids at high pressures, but from a practical standpoint, the fact that this feature is predicted by MELTS for fertile peridotite limits application of the standard relationships for triangular melting regimes (requiring a well-defined maximum melting pressure, P_0 ; Plank *et al.*, 1995) to MELTS calculations with $T_p < 1500^\circ\text{C}$. It is important to reemphasize that despite this limitation, the position of the solidus predicted by MELTS in both temperature and entropy (or potential temperature) space at pressures up to ~ 6 GPa is not unreasonable, even though the equations of state used for minerals and liquids were not intended to extrapolate so far. We show calculations with T_p up to this maximum for completeness and to further our understanding of the implications of this possible behavior of the solidus at high P , but the reader is cautioned that these calculations are extrapolated beyond any reasonable expectation of accurate prediction of actual phase relations.

The difficulty imposed by the inadequate treatment of Cr_2O_3 in MELTS (Hirschmann *et al.*, 1998b) is illustrated by Fig. 1. In the present version of MELTS, spinel is the only mantle phase that accepts Cr_2O_3 , whereas in natural systems, pyroxenes and garnet are significant Cr_2O_3 reservoirs. Hence when Cr_2O_3 is included in the calculation, spinel is stable under all subsolidus conditions and persists nearly to the liquidus (Fig. 1a and b). On the other hand, when Cr_2O_3 is excluded from the

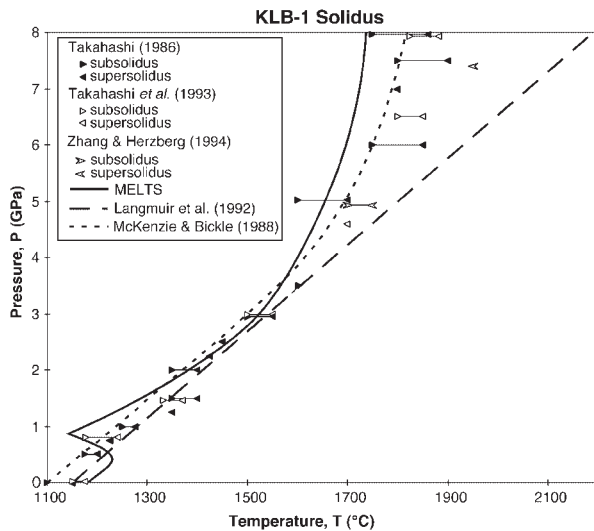


Fig. 2. Comparison of the solidus predicted by MELTS for composition KLB-1 (Takahashi, 1986) with model peridotite solidi of Langmuir *et al.* (1992) and McKenzie & Bickle (1988) and experimental brackets on the solidus of KLB-1 (Takahashi, 1986; Takahashi *et al.*, 1993; Zhang & Herzberg, 1994). Right arrows are liquid-free experiments, left arrows are liquid-bearing experiments, and paired brackets are linked by continuous lines.

composition, as in Fig. 1c and d, spinel is insufficiently stable and hence the garnet–spinel and spinel–plagioclase transition regions are artificially narrow and spinel disappears from the residue before cpx, near 10% melting. We have tried to work around this problem using duplicate calculations in Cr-bearing and Cr-absent compositions. When similar behavior is observed in both cases, we infer that errors in spinel stability are not seriously affecting our results.

Previous attempts to estimate liquid compositions during isentropic batch melting have generally chosen a path through a chemistry function [i.e. liquid composition as a function of (P , F) or (P , T)] fitted to isobaric melting data, where the path is set by the independently estimated melting function or productivity, $-dF/dP$, or by an estimate of the thermal gradient during melting, dT/dP . For example, Klein & Langmuir (1987) illustrated the construction of such a model for SiO_2 as a function of F and P using isobaric curves (fits to experiments expressed as SiO_2 contents of partial melts of fertile peridotite vs F at constant P) and an estimated isentropic productivity of 1.2%/kbar (Fig. 3a; it should be noted that we retain units of %/kbar for consistency with previous work; 1%/kbar = 10%/GPa). In contrast, MELTS generates isentropic batch melting paths directly, without treating the chemistry and melting functions independently. The result (Fig. 3b) differs considerably from that of Klein & Langmuir (1987) (Fig. 3a) for two reasons. First, the isobaric melting curves are clearly different in that they show high SiO_2 at low F (Baker *et al.*, 1995), especially

at the low- P end of the spinel peridotite field (Hirschmann *et al.*, 1998a), a feature that was not apparent in experimental data as of 1987. Although this effect is clear in experiments of Baker *et al.* (1995), Kushiro (1996), and others, its magnitude is exaggerated by MELTS [for detailed comparison of MELTS compositions with isobaric experimental data, see Hirschmann *et al.* (1998b)]. Second, the isentropic productivity is not constant at 1.2%/kbar; instead, it systematically increases along each melting path from as little as 0.25%/kbar on the solidus to a maximum of $\sim 3\%$ /kbar at the exhaustion of cpx from the residue (Hirschmann *et al.*, 1994; Asimow *et al.*, 1997). These two novel aspects combine to predict concave-up isentropic batch melting paths in Fig. 3b, in contrast to Klein & Langmuir's concave-down paths. We emphasize, however, that although this figure is useful for building intuition in that it connects isobaric melting to the less familiar isentropic paths, it is probably not directly relevant to MORB petrogenesis, because the consequences of fractional melting on liquid and residue compositions are predicted to be significant (see below). Thus the idea of using batch melting isobars or isentropes to predict compositions from fractional fusion is less useful than was once thought (Klein & Langmuir, 1987; McKenzie & Bickle, 1988).

INCREMENTALLY ADIABATIC FRACTIONAL MELTING

Fractional melting cannot be a locally isentropic process, in that escaping melts remove entropy from the system. Here we model fractional melting as an idealized process of infinitesimal isentropic batch melting steps followed by extraction of all liquid formed (see Asimow *et al.*, 1995, 1997). The composition and entropy of the residue of each step then serves as the reference for the next increment. The extension to continuous fusion, where some amount of melt remains behind after each step, is straightforward (Asimow *et al.*, 1997).

Most previous attempts to construct models of polybaric fractional melting have been linked closely to melt compositions and melt fractions from batch melting experiments on a limited number of peridotite bulk compositions. Those that use compositions directly from batch melting experiments (Klein & Langmuir, 1987; McKenzie & Bickle, 1988; Watson & McKenzie, 1991; Iwamori *et al.*, 1995) include none of the compositional effects of fractional melting and any differences between batch and fractional fusion reflect largely *ad hoc* estimates of the differences in productivity and P – T paths between batch and fractional melting. Other parameterizations use major element partition coefficients fitted to batch melting experiments (Niu & Batiza, 1991; Langmuir *et al.*, 1992) or four-phase saturation surfaces (Kinzler &

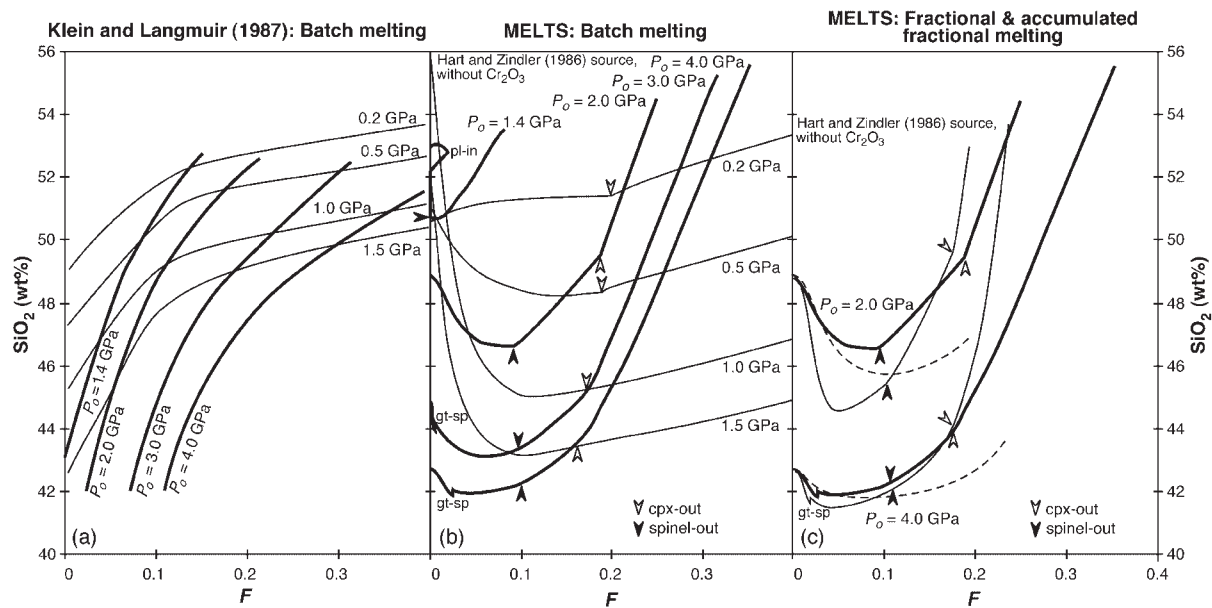


Fig. 3. SiO_2 in silicate liquids from melting of peridotite vs extent of melting, F . (a) Fits to isobaric batch melting data and estimated polybaric paths from Klein & Langmuir (1987). Light curves are isobaric paths at the labeled pressures. Bold curves are isentropic paths beginning at the labeled solidus intersection pressure P_o assuming a productivity, $-dF/dP$, of 1.2%/kbar. (b) MELTS predictions for isentropic batch melting of Cr-free Hart & Zindler (1986) composition (HZ_noCr). (Note that the $P_o = 1.4$ GPa path intersects the spinel–plagioclase transition and freezes completely before melting resumes in the plagioclase peridotite field.) Kinks on the polybaric paths occur at the garnet–spinel peridotite transition on the $P_o = 3.0$ and $P_o = 4.0$ GPa paths and at the exhaustion of spinel at $F \sim 0.09$ and the exhaustion of cpx at $F \sim 0.18$ on all paths. (c) Adiabatic (incrementally isentropic) fractional melting according to MELTS: incremental melt compositions are shown as light continuous curves, integrated fractional melts are shown as light dashed curves. F in all these cases is unity minus the mass fraction of the original solid remaining. The batch melting paths from (b) are shown for comparison as bold continuous lines; the integrated fractional melts are substantially different from batch melting both in that lower melt fractions are achieved and SiO_2 content follows a different path. Kinks correspond to phase exhaustion as in (b).

Grove, 1992a, 1992b; Kinzler, 1997): within the fitted range, these parameterizations try to account for the evolution of residue composition and variations in liquid composition with progressive fractional fusion. However, all these approaches have depended on poorly constrained (and largely non-thermodynamically grounded) estimates of productivity and P – T paths for fractional fusion. The incremental batch experimental approach of Hirose & Kushiro (1998) attempted to approximate the P – T – F path of incrementally adiabatic polybaric fractional fusion; although this approach is a promising one, it involves relatively large step sizes (i.e. the first increment is 6.5% melting), so it is not a good approximation to pure fractional fusion.

Figure 3c illustrates the likely magnitude of the differences between batch and fractional melting based on MELTS calculations. Conventional petrological wisdom holds that integrated fractional melts are similar to batch melts, but this is strictly true only for highly incompatible elements and only when partition coefficients are constant. In this polybaric case, however, where productivity is different for batch and fractional processes and where SiO_2 partitioning depends strongly on pressure (O'Hara, 1968), batch and integrated fractional melts are very

different, and the differences generally increase with F (i.e. with the pressure range from solidus to the pressure of comparison). The modeled differences shown in Fig. 3c are qualitatively similar to the results of Hirose & Kushiro (1998). Any melting model where the melt composition changes with pressure will yield such a difference between polybaric batch melting and integrated polybaric fractional fusion; such an effect is clear, for instance, in FeO^* values in the model of Langmuir *et al.* (1992). The magnitude of the differences between batch and fractional melting from a given model, however, is sensitively dependent on the productivity function. As we will see below, in an adiabatic melting column, MELTS calculations produce the bulk of liquid mass over a smaller range of pressure than models with nearly linear productivity and hence predict smaller differences in SiO_2 and FeO^* concentrations between batch and accumulated fractional liquids.

MEAN PROPERTIES OF MELTING REGIMES

Two-dimensional models of mid-ocean ridge melting can often be simply characterized by mean properties: e.g.

the mean pressure of extraction (\bar{P}), the mean extent of melting F_B (see Plank *et al.*, 1995), or the total crustal thickness (Z_c , when given in units of kilometers, or P_c , the pressure at the base of the crust). For any model (e.g. active or passive, batch or fractional), the relationships between these average properties and the physical parameters of the model (e.g. P_o or P_f) depend on the productivity and the form of its variations with F , P_o , and source composition; i.e. the nonlinear melting function (or, equivalently, non-constant $-dF/dP$) predicted by thermodynamics (Asimow *et al.*, 1997) results in nonlinear relationships among P_o , P_f , \bar{P} , F_B , and $(Z_c)^{1/2}$. We show below the relationships among all these variables according to the MELTS model and, for comparison, the models of Langmuir *et al.* (1992) and Kinzler (1997), all for the reference case of perfect fractional melting and passive flow for the Hart & Zindler (1986) source composition.

Formalisms for obtaining mean properties of melts produced by 2D model melting regimes using 1D melting models have been presented several times (Klein & Langmuir, 1987; McKenzie & Bickle, 1988; Plank & Langmuir, 1992; Richardson & McKenzie, 1994), but the issue requires clarification for a model such as ours with strongly varying productivity, as some of the prior treatments apply only to special cases. There is agreement that the mean melt composition, C , produced along each streamline or evaluated at each point along the exit boundary of the melting regime is obtained from a single integration,

$$C = \frac{1}{F} \int_0^F c \, dF' \quad (1)$$

(McKenzie & Bickle, 1988), but the meaning of c , defined as the composition of the melt added to increase the fraction of melt from F to $F + dF$, is obvious only for fractional melting, where it is the instantaneous melt composition produced by each increment of melting, dF . For batch melting and intermediate processes (e.g. 'continuous' or 'dynamic' melting with a retained porosity above which melts are fractionally removed; Johnson & Dick, 1992; Langmuir *et al.*, 1992), this definition requires that c is the net transfer of components between solid and liquid, such that for batch melting C is the instantaneous liquid in equilibrium with the residue.

For end-member active flow, all streamlines and points on the exit boundary of the melting regime are the same (Plank *et al.*, 1995), and equation (1) is all that is needed to compute the mean output of the melting column. Some models of aggregate MORB composition have considered only this column average (Niu & Batiza, 1991), but for flows with some 2D character to the exit boundary of the melting regime (e.g. the passive flow

triangle), another step is required. McKenzie & Bickle (1988) defined the 'point and depth average', the mean composition of all melts exiting the melting regime, by integration with respect to depth z from the solidus ($z = 0$) to the height of the residual mantle column h :

$$\bar{C} = \frac{\int_0^h CF \, dz}{\int_0^h F \, dz} \quad (2)$$

where C is the 'point average' from equation (1); in contrast, Klein & Langmuir (1987) and Langmuir *et al.* (1992) averaged with respect to F :

$$\bar{C} = \frac{\int_0^{F_{\max}} CF \, dF}{\int_0^{F_{\max}} F \, dF} \quad (3)$$

For calculations using discrete intervals equally spaced in P or in z , or for the case of constant productivity, these definitions produce identical results. For calculations discretized in F where $-dF/dP$ is not constant, however, they differ. For example, for a variable- P_f melting regime, where F_{\max} is achieved at some pressure P_f but corner flow continues to a lower pressure (perhaps P_c), giving a trapezoidal melting regime, (3) cannot describe the part of the residual mantle column between P_f and P_c that is characterized throughout by $F = F_{\max}$.

The relationship between (2) and (3) is revealed in the derivation of Plank & Langmuir (1992), who gave the more general equation

$$\bar{C} = \frac{\int_0^{F_{\max}} CF v_x \left(\frac{dz}{dF} \right) dF}{\int_0^{F_{\max}} F v_x \left(\frac{dz}{dF} \right) dF} \quad (4)$$

where v_x is the horizontal velocity of the residue at a given depth in the residual mantle column. The value of v_x is most simply assumed to be independent of depth

(e.g. Klein & Langmuir, 1987; McKenzie & Bickle, 1988; McKenzie & O’Nions, 1991; Langmuir *et al.*, 1992), although this is not the result of the simplest, constant-viscosity corner-flow model (Batchelor, 1967). If v_x is held constant, it cancels out of (4), and it is clear that (4) and (2) are equivalent. Equation (3), however, is a special case for constant v_x and dz/dF ; constant dz/dF corresponds to constant spacing in depth of the melt fraction contours, or approximately to constant productivity, $-dF/dP$. The difficulty of using (4) in regions where productivity is zero (hence dz/dF is infinite), such as the shallow mantle above a variable- P_f melting regime, is clear. As z is not well characterized in our calculations (Asimow & Stolper, 1999), whereas P is known exactly as an independent variable, mean properties for all passive-flow models are calculated in this work according to

$$\bar{C} = \frac{\int_{P_o}^{P_c} CFdP}{\int_{P_o}^{P_c} FdP} \quad (5)$$

which assumes constant v_x and is in practice nearly identical to (2). The mean pressure is calculated similarly, replacing C in the numerator of (5) with P for batch melting and with the column or streamline average $P' = 1/F \int_0^F PdF'$ for fractional melting. The mean melt fraction is calculated from

$$F_B = \frac{\int_{P_o}^{P_c} FdP}{\int_{P_o}^{P_c} dP} = \frac{\int_{P_o}^{P_c} FdP}{P_c - P_o} \quad (6)$$

In equations (5) and (6) we use P_c as the upper limit of integration, reflecting the idea that the residual mantle column and the mantle corner flow extend to the base of the crust.

For cases where melting stops at $P_f > P_c$, whether as a result of imposed cooling or productivity effects, the value of F at P_f , F_{max} , applies throughout the interval P_f to P_c , which simulates a trapezoidal melting regime contained within a triangular corner-flow field,

$$F_B = \frac{\int_{P_o}^{P_f} FdP + F_{max}(P_c - P_f)}{P_c - P_o} \quad (7)$$

Likewise, the integrals for mean pressure and mean composition when $P_f > P_c$ use the values of P' and C that obtain at P_f for the entire interval P_f to P_c . It should be noted that all these forms are based on the assumption that the flow is incompressible (they are therefore equivalent to integration with respect to the stream function; Richardson & McKenzie, 1994) and hence that even if liquids are removed from chemical equilibrium with the residue in the interior of the melting regime they are physically carried along solid-flow streamlines to the boundaries of the melting regime (with only a Boussinesq effect on the fluid dynamics). A truly rigorous model of mixing requires a mass-conservative calculation of the liquid and solid flow fields allowing for compaction (e.g. Spiegelman, 1996).

The effects of productivity functions on extent of melting, mean extent of melting, and crustal thickness are explored in Figs 4–6. Figure 4 emphasizes the progress of F and its pressure derivative and integral along each adiabat from the solidus to the base of the crust, independent of the mixing function or the shape of the melting regime. Figure 5 illustrates variable- P_o systematics by showing the final melt production by adiabats of differing potential temperature (or P_o) where P_f is equal to the base of the crust P_c (i.e. the melting regime is triangular). Figure 6 illustrates variable- P_f systematics, showing the total output when melting stops at various values of P_f , but the integration continues at the final value of F all the way to the base of the crust (i.e. the melting regime is trapezoidal and the residual mantle column contains equally depleted material from the base of the crust all the way down to P_f).

Productivity functions

In Fig. 4, the output of the MELTS model is compared with the parameterization of Langmuir *et al.* (1992), which has a slight decrease in productivity with decreasing pressure (a linear correction of 10 parts in 88 per GPa as a result of convergence of the liquidus and solidus) superimposed on a small (~20%), discontinuous decrease in productivity at the depth of cpx exhaustion. Figure 4a and b shows the productivity functions of the two models vs pressure for melting paths with $P_o = 1.3, 1.7, 2.1, 2.7,$ and 4.4 GPa. The strongly increasing productivity leading up to cpx-out along each path in the MELTS model (Hirschmann *et al.*, 1994; Asimow *et al.*, 1997) is prominent in Fig. 4a, which also shows the following

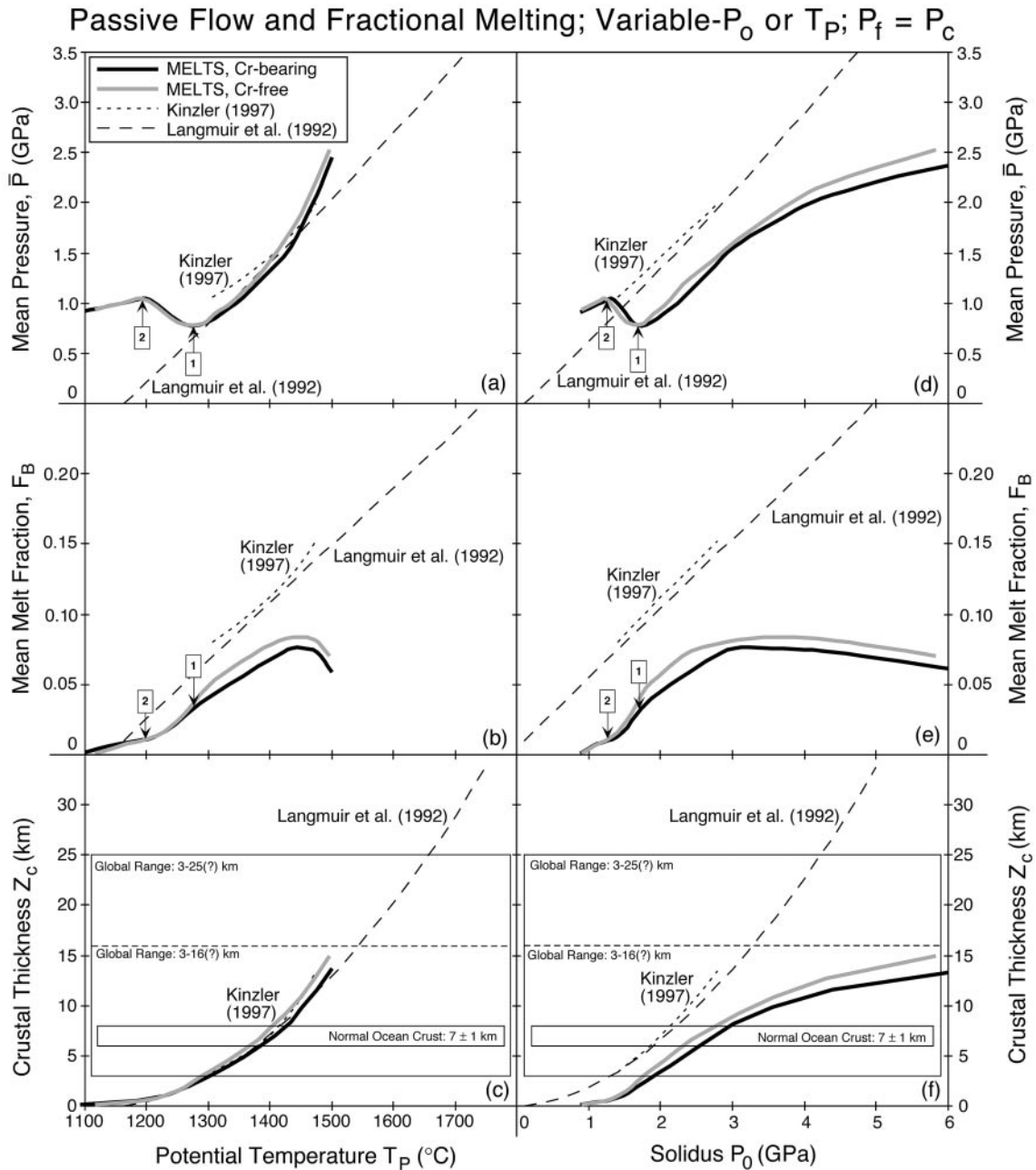


Fig. 5. Mean properties of 2D integrated melting regimes as functions of potential temperature and initial pressure of melting assuming passive flow, with the final pressure of melting, P_f , assumed to be at the base of the crust (i.e. variable- P_0 systematics). MELTS results are compared with the models of Langmuir *et al.* (1992; long-dashed line) and Kinzler (1997; dotted line) as representatives of a class of published models with nearly constant productivity. The input proportions of all oxides considered by each model were set to the Hart & Zindler (1986) source composition. MELTS calculations for both the Cr-bearing (heavy continuous curves) and Cr-free (heavy shaded curves) source compositions are shown. (a) Mean pressure, \bar{P} , vs potential temperature, T_P . (b) Mean melt fraction, F_B (see Plank *et al.*, 1995), vs T_P . (c) Crustal thickness, Z_c , calculated according to the formalism of Klein & Langmuir (1987), vs T_P . The normal oceanic crustal thickness range of 7 ± 1 km is shown, as is the global range of oceanic crustal thickness from a minimum of ~ 3 km to a maximum at Iceland, where crustal thickness estimates range from 14 to 25 km or more. (d) \bar{P} vs solidus intersection pressure, P_0 . (e) F_B vs P_0 . (f) Z_c vs P_0 . Boxed 1 indicates the maximum T_P or P_0 for plagioclase to appear in the residue; 2 indicates the minimum T_P or P_0 for melting to occur between the appearance of residual plagioclase and the base of the crust.

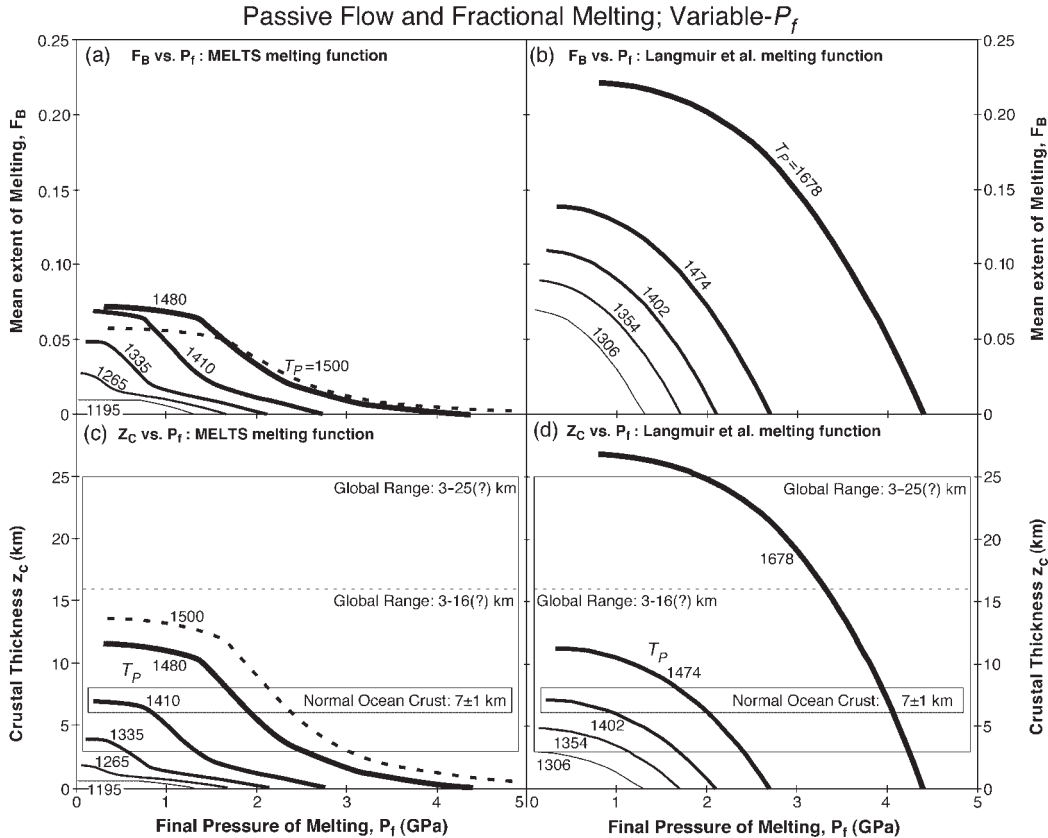


Fig. 6. Variations of mean properties of the melting regime with variations in the final pressure of melting (P_f) for passive flow and the Cr-bearing Hart & Zindler (1986) source composition (HZ) according to MELTS and Langmuir *et al.* (1992). The same five potential temperatures are shown as in Fig. 4, although the intent is to see how calculated mean properties correlate with P_f if T_P is constant. For MELTS output the extreme case of $P_o = 6.4$ GPa ($T_P = 1500^\circ\text{C}$) is also shown, dashed. The integrations underlying these curves assume a trapezoidal melting regime, with the upper part of the residual mantle column from P_i to P_c all characterized by F_{max} . (a) and (b) show F_B vs P_f . (c) and (d) show crustal thickness, z_c , vs P_f ; the ranges of z_c thought to occur in nature are indicated as in Fig. 5. The crossing of curves in (a) is related to the maximum in F_B for variable- P_o melting regimes that have the productivity functions output by MELTS (Fig. 5e): i.e. when $P_o = 6.4$ GPa, the solid flux into the melting regime is much larger than when $P_o = 2.7$ GPa because the width of the base of the triangular melting regime increases with P_o , but the limits on F (i.e. growth of the low-productivity tail into the garnet field; the increase in size of cpx-absent melting regime; and the lower overall productivity with increasing P_o) lead to a melt-flux out of the hotter melting regime only slightly larger and hence the unintuitive result that the ratio of melt-flux-out to solid-flux-in (F_B) can be smaller for the hotter melting regime.

The productivity functions ($-dF/dP$) shown in Fig. 4a and b are integrated to produce the F vs P plots in Fig. 4c and d for the MELTS and Langmuir *et al.* (1992) models. The mean F and mean P for variable- P_o systematics [i.e. using (6) and (7) and integrating to $P_f = P_c$] are shown by a filled circle along each F vs P curve. Comparing these plots shows three important differences between these models. First, because of the low productivity in the early stages of melting according to MELTS, there is a ‘tail’ 1–2.5 GPa wide in which F remains low. Second, as the shape of the F – P curve in the Langmuir *et al.* (1992) model is almost independent of P_o , the mean melt fraction, F_B , increases almost linearly with P_o to values of at least 0.22. In the MELTS model, however, there is a maximum in F_B at ~ 0.08 . This behavior is explored in more detail below. Third, the

maximum F achieved by the Langmuir *et al.* (1992) model increases essentially without bound, whereas fractional melting with MELTS would require extraordinarily deep P_o and high T_P to reach F_{max} more than a few percent higher than that achieved at cpx-out. Instead, in the MELTS model the lengthening of the tail, the decrease in F at cpx-out, and the overall lower productivity at equal F associated with increasing P_o all combine to yield F_{max} in the narrow range 0.18–0.22 at the base of the crust over the wide range in P_o of 2.7–4.4 GPa (Fig. 4c).

The extent of melting functions shown in Fig. 4c and d are integrated to yield the $\int FdP$ curves in Fig. 4e and f. For these plots, the upper limit of integration is varied along the P -axis from P_o to P_c to generate the curves shown. For passive flow models that aggregate all liquids to form the crust, this integral is equal to the pressure at

the base of the crust and so is related to crustal thickness by a simple density correction. Assuming a constant crustal density of 2.62 g/cm^3 , we obtain crustal thickness in kilometers according to the formalism of Klein & Langmuir (1987). These figures, like the F - P plots, show that any given crustal thickness is produced by a melting path with much higher P_o according to MELTS than according to the Langmuir *et al.* (1992) model. For example, 7 km of crust results from an adiabat with $P_o \sim 2.1 \text{ GPa}$ in the Langmuir *et al.* (1992) model but requires $P_o \sim 2.8 \text{ GPa}$ according to MELTS. These figures also show that the Langmuir *et al.* (1992) model can readily generate crustal thickness of 30 km or more. MELTS, on the other hand, at least for the passive-flow case, never achieves values greater than $\sim 15 \text{ km}$ within the range of P_o limited by the T_p maximum on the solidus discussed above (active flow and other means of generating more crust are discussed below).

Variable- P_o systematics

Figure 5 presents the net melt production of melting regimes at the final pressure of melting, whereas Fig. 4 shows the evolution of melting with pressure through each melting regime. Results are shown for passive-flow fractional melting calculations with variable- P_o systematics: P_f is adjusted to be equal to the base of the crust for each P_o (i.e. melting stops in each column at $P = \int_{P_o}^P F dP$) and P_o varies with T_p . The relationships among the plotted variables are controlled by the shape of the solidus (i.e. P_o as a function of T_p ; see Fig. 1a and c), variations of productivity among melting paths of different potential temperature (Fig. 4a and b), and variations of productivity with F along the melting path at a given potential temperature (insets in Fig. 4a and b). As shown by Klein & Langmuir (1987), any model with a linear solidus (in P - T_p space) and constant productivity will yield linear relationships among T_p , P_o , \bar{P} , F_b , and $(\zeta_c)^{1/2}$. The productivity variations in the model of Langmuir *et al.* (1992) are small enough that in Fig. 5 the relationships for this model are indistinguishable from straight lines for \bar{P} and F_b and parabolas for ζ_c when plotted against both P_o and T_p . The model of Kinzler (1997) assumes constant productivity, also resulting in linear relations among P_o , \bar{P} , F_b , and $(\zeta_c)^{1/2}$ (Fig. 5d-f), despite predicting a mildly curved solidus that leads to weakly curved trends in these variables against T_p (Fig. 5a-c). There is no simple way to combine plagioclase-, spinel-, and/or garnet-bearing calculations using the Kinzler (1997) model, so results are shown only for melting paths with residual spinel everywhere.

Results of MELTS calculations for both the Cr-bearing and Cr-absent source compositions are shown in Fig. 5;

the results for both compositions are similar in all important respects (i.e. the following discussion is not sensitive to details of spinel stability). When plotted against potential temperature, the MELTS results and the models of Langmuir *et al.* (1992) and Kinzler (1997) agree in many respects in the 'normal' range of potential temperatures (i.e. 1300 – 1400°C), but differ for anomalously hot or cold mantle. When plotted against P_o , MELTS predicts lower F_b and ζ_c for all P_o for reasons discussed above, but primarily because MELTS generates a low-productivity 'tail' near P_o (Hirschmann *et al.*, 1994; Asimow *et al.*, 1997); hence for $P_o \sim 1.5$ – 3 GPa , MELTS calculations mimic a constant-productivity model with P_o at least 0.5 GPa lower. The differences for abnormally cold conditions are not surprising given the novel behavior predicted by MELTS for low F (which shows up most strongly in integrated melts with low F_b) and the influence of the spinel-plagioclase transition. At hotter than normal potential temperatures, the F_b value attained by MELTS for increasing P_o flattens and reaches a maximum for $P_o \sim 3.5 \text{ GPa}$, which in turn leads to a decreasing slope of the crustal thickness vs solidus pressure curve beyond $P_o \sim 3.0 \text{ GPa}$: that is, from simple 2D passive-flow fractional melting regimes of this type with a well-defined P_o , MELTS cannot generate crustal thickness above 15 km , regardless of T_p .

For solidus pressures greater than $\sim 1.7 \text{ GPa}$, i.e. potential temperatures higher than $\sim 1280^\circ\text{C}$ (boxed 1 in Fig. 5), plagioclase does not appear in the residue during fractional melting (this value of T_p is lower than the limit for plagioclase to appear on batch melting adiabats; boxed 5 in Fig. 1). As solidus pressure decreases from 1.7 GPa ($T_p < 1280^\circ\text{C}$, boxed 1 in Fig. 5), the spinel-plagioclase peridotite transition plays an increasingly important role in modifying the amount of melt produced and the pressure range over which melt production occurs. In a simple passive flow model, this transition first divides the melting region into two disconnected regions, an upper triangle and a lower trapezoid (Asimow *et al.*, 1995). With falling potential temperature, the bottom of the triangle retreats upward and the top of the trapezoid retreats downwards, i.e. the transition shuts off melting at deeper levels and melting resumes at shallower levels (see solidus in Fig. 1) as P_o and T_p decrease. This effect is manifested in Fig. 5d as a turnaround in mean pressure of melting (i.e. the loss of the shallower parts of the melting region results in increasing mean pressures of melting with falling potential temperature or solidus pressure in this range). At a certain critical value of T_p and P_o (the kink labeled with boxed 2 in the Fig. 5 curves at $T_p \sim 1200^\circ\text{C}$ and $P_o \sim 1.3 \text{ GPa}$), the upper triangle of the melting regime disappears; i.e. the pressure at which melting in the plagioclase field would resume becomes shallower than the minimum pressure of melting at the base of the crust. With further

falls in T_p , the lower trapezoid shrinks and finally disappears at $T_p \sim 1100^\circ\text{C}$ (the cusp on the solidus, point labeled with boxed 1 in Fig. 1); lower values of T_p produce no melt. The details of this low- T_p behavior depend on the particular near-solidus relations predicted by MELTS, but general features such as the division of a fractional melting regime into disconnected parts are a necessary consequence of the thermodynamics of plagioclase formation (Asimow *et al.*, 1995).

For hotter mantle, the differences between MELTS and the other models considered are due both to the different model solidus curves (which determine the relationship between potential temperature and the pressure at which melting begins; see Figs 1 and 2) and to the different model productivity functions. Although the decrease in productivity beyond the exhaustion of cpx poses a significant limitation to the achievement of high F , this is a minor factor in the behavior of F_B and ζ_c at high potential temperatures for variable- P_o passive-flow regimes because it occurs near the apex of the triangular melting zone and has little weight in the integrals. Instead, the flattening of the MELTS-calculated (and experimentally determined) solidus at high T_p (see Fig. 2) dominates. The slope of the solidus controls both the vertical extent of the melting regime (i.e. $P_o - P_f$) and, in the high- T_p range, the productivity differences between adiabats of differing potential temperature (see inset to Fig. 4a). As the solidus modeled by MELTS becomes nearly vertical [i.e. $(dT_p/dP)_{\text{solidus}}$ approaches zero] beyond 4.0 GPa (see Fig. 2), the productivity at the solidus approaches zero, with the net result that the vertical extent of the melting regime increases rapidly for small rises in T_p without significant increase in total melt production. As F_B is defined as total melt production divided by $(P_c - P_o)$, the flattening solidus and the low productivity it implies combine to give a maximum in F_B and a plateau in ζ_c plotted against P_o (Fig. 5e and f). On the other hand, when crustal thickness, which is proportional to the product of F_B and $(P_c - P_o)$, is plotted against T_p instead of P_o , the effects of solidus curvature on $(P_c - P_o)$ and productivity approximately cancel and the MELTS curves in Fig. 5c closely resemble the Langmuir *et al.* (1992) and Kinzler (1997) models.

The region above 3–4 GPa where the solidus slope becomes low enough to have large effects comes into play for dry peridotite melting and normal oceanic crustal thickness (i.e. 7 ± 1 km) only because of the generally low average productivity predicted by MELTS near the solidus at any pressure (Hirschmann *et al.*, 1994, 1999a; Asimow *et al.*, 1997), which is also responsible for the ≤ 0.5 GPa offset at normal oceanic crustal thickness between the MELTS and Langmuir *et al.* (1992) curves for crustal thickness against solidus pressure in Fig. 5f. It should be noted that at given P , the low polybaric productivity, $-dF/dP$, at low F according to MELTS

results largely from the prediction of low isobaric productivity $(\partial F/\partial T)_p$ near the solidus (i.e. $F < 0.03$); although plausible [and especially so if small amounts of water are present (Hirth & Kohlstedt, 1996)], this feature of MELTS calculations remains to be experimentally verified or disproved at any pressure (Hirschmann *et al.*, 1999a).

Little confidence should be placed in the quantitative results of either MELTS or the other parameterizations beyond $P_o \sim 3.0$ GPa given the paucity of experimental data on peridotite melting at these pressures and the low-order equations of state used in MELTS. The experimental data on the position of the peridotite solidus at high pressure (Fig. 2), however, do suggest that the type of systematics predicted by MELTS in Fig. 5, in particular the difficulty in generating significant increases in the mean melt fraction and crustal thickness without very large increases in the initial depth of melting, may be closer to reality than those predicted by models based on a linear or nearly linear solidus, which suggest simple continuations of highly productive lower-pressure melting. Seismic data (Zhang *et al.*, 1994; MELT Seismic Team, 1998) support the notion that melting at normal ridges does extend to considerable depths (>6 GPa), although the seismic velocity may be imaging ‘incipient melting’ as a result of the presence of water in the source (McKenzie & Bickle, 1988; Hirth & Kohlstedt, 1996; Hirschmann *et al.*, 1999a). Qualitatively, however, one should expect similar effects on F_B (and hence incompatible trace element concentrations) and crustal thickness as functions of P_o from any mechanism that substantially increases the depth interval of the melting regime without increasing the total extent of melting very much (i.e. whether it is due to the flattening of the dry solidus at high pressures or to the presence in the source of water or other incompatible components).

Although the MELTS model cannot readily generate large crustal thickness given a simple triangular passive flow geometry, this may reflect the shortcomings of strictly passive-flow models rather than of MELTS. The behavior at high P_o of any simple triangular ridge model (i.e. of the type on which the calculations shown in Fig. 5 were based) is a result of the end-member passive flow mixing function underlying the evaluation of F_B . This formalism requires perfect melt extraction from all parts of the triangular melting regime no matter how large it becomes, and thus it implies increasingly unreasonable physical assumptions as P_o increases (Spiegelman & McKenzie, 1987). Consequently, modeling of very hot (or wet) mantle regions must incorporate reasonable fluid-dynamical melt-flow models. Furthermore, many workers have argued that Iceland, in particular, has a component of active upwelling as a result of the Iceland plume that brings more mantle through the melting regime than a triangular passive flow geometry (Korenaga *et al.*, 2000),

at least below the rheological boundary layer (Ito *et al.*, 1999).

Variable- P_f systematics

Figure 6 presents calculated variations in mean extent of melting and crustal thickness in melting regimes controlled by the final pressure of melting, as envisioned by Shen & Forsyth (1995) and Niu & Hékinian (1997*b*), using both the MELTS and Langmuir *et al.* (1992) models, for five values of P_o . For example, the uppermost continuous curve in Fig. 6a represents the average extent of melting (F_B) calculated by MELTS for a case where melting begins at 4.4 GPa and continues to a P_f ranging from 4.4 GPa down to that at the base of the crust; the prominent downward kink on this curve at ~ 1.4 GPa represents the productivity drop at the exhaustion of cpx from the residue. The Langmuir *et al.* (1992) curves in Fig. 6b closely resemble the form expected for constant productivity. The overall downward-concavity of these curves is the result of the triangular geometry of the melting regime such that increasing P_f first cuts off the small tip of the triangle and results in only a small decrease in F_B . In the regions where productivity strongly increases with decreasing P_f , the MELTS melting function overwhelms this general downward curvature and produces regions of upward concavity in Fig. 6a. Only after cpx exhaustion, when the MELTS productivity function is nearly constant, does the F_B vs P_f curve obtain the constant-productivity (i.e. concave-down) shape. Nevertheless, except for the kink in the MELTS curves at cpx-out, the results of these plots are qualitatively similar for both models: a given increase in P_f as a result of conductive cooling has negligible effect on F_B for the first ~ 0.5 GPa below P_o , and then becomes increasingly effective in reducing F_B (and crustal thickness, see below) as P_f reaches wider portions and/or the extremely productive part of the triangular melting regime.

Figure 6c and d addresses the issue of the range in potential temperatures sampled by oceanic ridges. Assuming melting to the base of the crust in all cases, Klein & Langmuir (1987) estimated the total range from the Cayman Trough (crustal thickness ~ 3 km) to Iceland (crustal thickness 10–16 km, Klein & Langmuir, 1987; or 16–25 km, Langmuir *et al.*, 1992) at 250°C (on compositional grounds as well as crustal thickness considerations), whereas Shen & Forsyth (1995) constructed a model to explain the global range of major element and crustal thickness variations in MORB, excluding hotspot-affected regions such as Iceland, with a temperature range of $<60^\circ\text{C}$ and substantial variations in the final pressure of melting. Whether any disagreement actually exists between these views depends on the nature of hotspots and hotspot-affected ridges. If hotspot-affected

ridges have high T_p but otherwise resemble ordinary ridge segments in flow geometry and in source chemistry (insofar as it affects the position of the solidus and the productivity of melting), then the type of estimate performed by Klein & Langmuir is a valid estimate of the global potential temperature range. If, however, hotspot-affected ridges have more active flow geometry, in either two or three dimensions, or source variations that lead in themselves to large variations in the solidus and productivity functions, then application of any one-parameter model to all ridge segments including Iceland will give misleading results. The existence of an ~ 100 km diameter low-velocity column under the center of Iceland, where crustal thickness reaches or exceeds 35 km [see compilation of Menke (1999)], has been observed seismically (Wolfe *et al.*, 1996). Along the neo-volcanic zone, crustal thickness above 30 km is roughly restricted to the region above the low-velocity column, decreasing from this maximum along strike both to the north and south and reaching 11 km at the shoreline of the Reykjanes Peninsula (Menke, 1999). There is no simple way to locate a boundary between a 'ridge-like' flow regime and a 'hotspot-like' flow regime, either in terms of intensity of active flow in the across-strike plane or the magnitude of plume-driven along-axis flow. Thus there is no clear indication what value of crustal thickness is the maximum one should seek to generate by ridge-like flow in defining the maximum T_p of the ridge system. We use a range from 16 to 25 km for this maximum, but neither this bound nor its significance is well defined.

Given a choice for the range in crustal thickness associated with the ridge system, the necessary range of final pressures of melting and the interplay between the choice of a global range for P_f and the implied global range in T_p (or the converse) remain model dependent and have not been well quantified. Although the shapes of the crustal thickness vs P_f curves according to MELTS and Langmuir *et al.* (1992) are different (compare Fig. 6c and d), the net results are broadly similar. Beginning with the case of a globally constant potential temperature for non-hotspot-influenced ridges (pure variable- P_f systematics), if we judge that normal 7 km ocean crust should result when $P_f = 0.2$ GPa (i.e. the base of the crust), then a range of final melting pressures up to 1.3 GPa in MELTS ($T_p = 1410^\circ\text{C}$ curve in Fig. 6c) and 1.7 GPa in Langmuir *et al.* (1992) ($T_p = 1402^\circ\text{C}$ curve in Fig. 6d) is required to limit crustal thickness to 3 km. If non-hotspot affected areas can have crustal thickness up to 11 km, then P_f needs to be able to reach values of 2.5 GPa for either model to be limited to 3 km of crust ($T_p = 1480^\circ\text{C}$ curve in Fig. 6c and $T_p = 1474^\circ\text{C}$ curve in 6d). At the maximum potential temperature for 2D integration in MELTS, 1500°C ($P_o = 6.4$ GPa), a range in final melting pressures from 0.5 to 3 GPa generates a range in crustal thickness from 14 to 3 km.

When melting always continues to the base of the crust (i.e. variable- P_0 systematics), MELTS requires a temperature range of $\sim 200^\circ\text{C}$ to enclose a range in crustal thickness from 3 to ~ 14 km (Fig. 5c); i.e. comparable with the T_p range of 250°C estimated by Langmuir and his coworkers to generate a similar range in crustal thickness. McKenzie & Bickle's (1988) result, using a solidus close to the MELTS solidus and a productivity function with a maximum at the solidus, is also similar: a 160°C range for crustal thickness from 3 to 15 km and a 260°C range including hotspots with up to 27 km of crust. Although the thermal derivatives of seismic velocity are uncertain, a 200 – 250°C subsolidus temperature range is also consistent with S-wave velocity variations of $\sim 2\%$ that correlate with the global trend in MORB chemistry (Humler *et al.*, 1993). It should be noted that this $\sim 200^\circ\text{C}$ range in T_p corresponds in MELTS to a range of ~ 4 GPa (from 2 to 6 GPa) or ~ 120 km in P_0 (Fig. 5f), which is much greater than the 2 GPa (1.3–3.3 GPa) or ~ 60 km range in P_0 implied by a 250°C range of T_p in the model of Langmuir *et al.* (1992). This difference, as explained above, is the result of the different shapes of the solidus in MELTS and in the Langmuir *et al.* (1992) model (Fig. 2), with MELTS predicting a rapid increase in depth of initial melting and decrease in overall productivity above $T_p = 1450^\circ\text{C}$. McKenzie & Bickle (1988), using a solidus intermediate between these two models, required an intermediate P_0 range of 3 GPa (0.5–3.5) to generate the global crustal thickness range.

A range of intermediate models that allow variations in both potential temperature and final pressure exists between the extreme models of constant T_p and constant P_f considered in the preceding two paragraphs. Independent constraints on the physically possible range of final pressure of melting could be combined with a productivity model to distinguish variations of these two parameters. For example, conductive cooling to 3 GPa is probably unreasonable (e.g. Shen & Forsyth, 1992), although there is as yet no definitive model of the thermal environment under a ridge at various spreading rates that constrains how deep conduction can occur. If conductive cooling is limited to ~ 1 GPa (30 km), then the minimum potential temperature variation between 3 km and 14 km crust is $\sim 115^\circ\text{C}$ (i.e. ~ 1385 – 1500°C ; Fig. 6c) in MELTS. The minimum potential temperature variation is still $\sim 200^\circ\text{C}$ for the Langmuir *et al.* (1992) model because the first 1 GPa of conductive cooling has so little effect on crustal thickness (Fig. 6d). The restriction of much of the crustal production to an interval of less than ~ 1 GPa in the MELTS models (reflecting the high productivity approaching cpx-out) reduces the depth of conductive cooling required to explain the global range of crustal thickness (excluding hotspots) using intermediate cases with both P_f and T_p variations relative to the Langmuir *et al.* (1992) model. For example, if we seek

only to explain a 'normal' range from 3 to 8 km in crustal thickness, then a range in T_p of 60°C (Shen & Forsyth, 1995) is consistent with P_f ranging from 0 to 1 GPa in MELTS, compared with 0–1.3 GPa given by Langmuir *et al.* (1992). To explain the full range of crustal thickness (3–14 km) using a potential temperature range of 60°C , MELTS-based calculations then require conductive cooling to 1.65 GPa, and the Langmuir *et al.* (1992) model needs P_f as large as 2.4 GPa.

AGGREGATE PRIMARY MELT COMPOSITIONS

The number of free parameters in a model of MORB genesis using MELTS is small, but there is still a many-dimensional space of possible primary melt compositions. Here we show the effects of variations in P_0 , P_f , and source composition (along a 1D enrichment–depletion vector) for batch and fractional melting in active and passive flow regimes, i.e. three free parameters for each of four cases. We compare the results with the models of Langmuir *et al.* (1992) and Kinzler (1997), and seek to identify in each case the predictions of each model that are robust and the data that might be used to distinguish among the various models when their predictions differ. In some cases we use a hybrid model that applies the Langmuir *et al.* (1992) chemistry function along a P – T – F path output by MELTS. Although not a self-consistent calculation, this may help to identify which differences among the model outputs are due to differences in the chemical models and which are due to the productivity behaviors explored above. We do not attempt to compare with the parameterization of Niu & Batiza (1991), which contains no constraints at $F < 10\%$ or $P > 2$ GPa, no approximation of passive flow aggregation, and no thermodynamic basis for its productivity model.

Passive flow, variable P_0

Figure 7 presents MELTS-calculated Na_2O and FeO^* contents for aggregate melts from Cr-bearing and Cr-free sources as functions of P_0 , Z_c , F_B , and \bar{P} for fractional melting and passive flow with P_f held equal to crustal thickness. Results from the Langmuir *et al.* (1992), Kinzler (1997), and Langmuir–MELTS hybrid models are shown for comparison.

Na_2O is conventionally taken as an indicator of extent of melting (Dick *et al.*, 1984; Klein & Langmuir, 1987), and Fig. 7a shows that the three models agree reasonably well for moderate values of F_B . MELTS never reaches mean extents of melting above $F_B = 0.08$ and so is unable to produce $\text{Na}_2\text{O} < 2.6\%$ (liquid compositions

henceforth are all in weight percent) in a primary aggregate liquid from melting regimes of this type with this source composition. Furthermore, in MELTS, Na is too incompatible (Hirschmann *et al.*, 1998*b*); hence at the solidus and at low F_B (i.e. $F_B < 0.025$), Na_2O is too high in the MELTS results and significantly higher than in the model of Langmuir *et al.* (1992), which incorporates a more accurate partition coefficient for Na in cpx (D_{Na}). It is not possible to separate cleanly the direct chemical effect of the Na partitioning error from the indirect effect

of Na compatibility on the solidus and productivity structure predicted by MELTS. The relative sensitivity of these two effects, however, can be explored using the hybrid model that combines the productivity and temperature paths from MELTS with liquid chemistry from the Langmuir *et al.* model. This produces a Na_2O vs F_B curve subparallel to the Langmuir *et al.* curve, offset to lower Na_2O and/or lower F_B . The hybrid model inherits the low F_B of the MELTS productivity function and the low Na_2O of the Langmuir cpx D_{Na} and so is

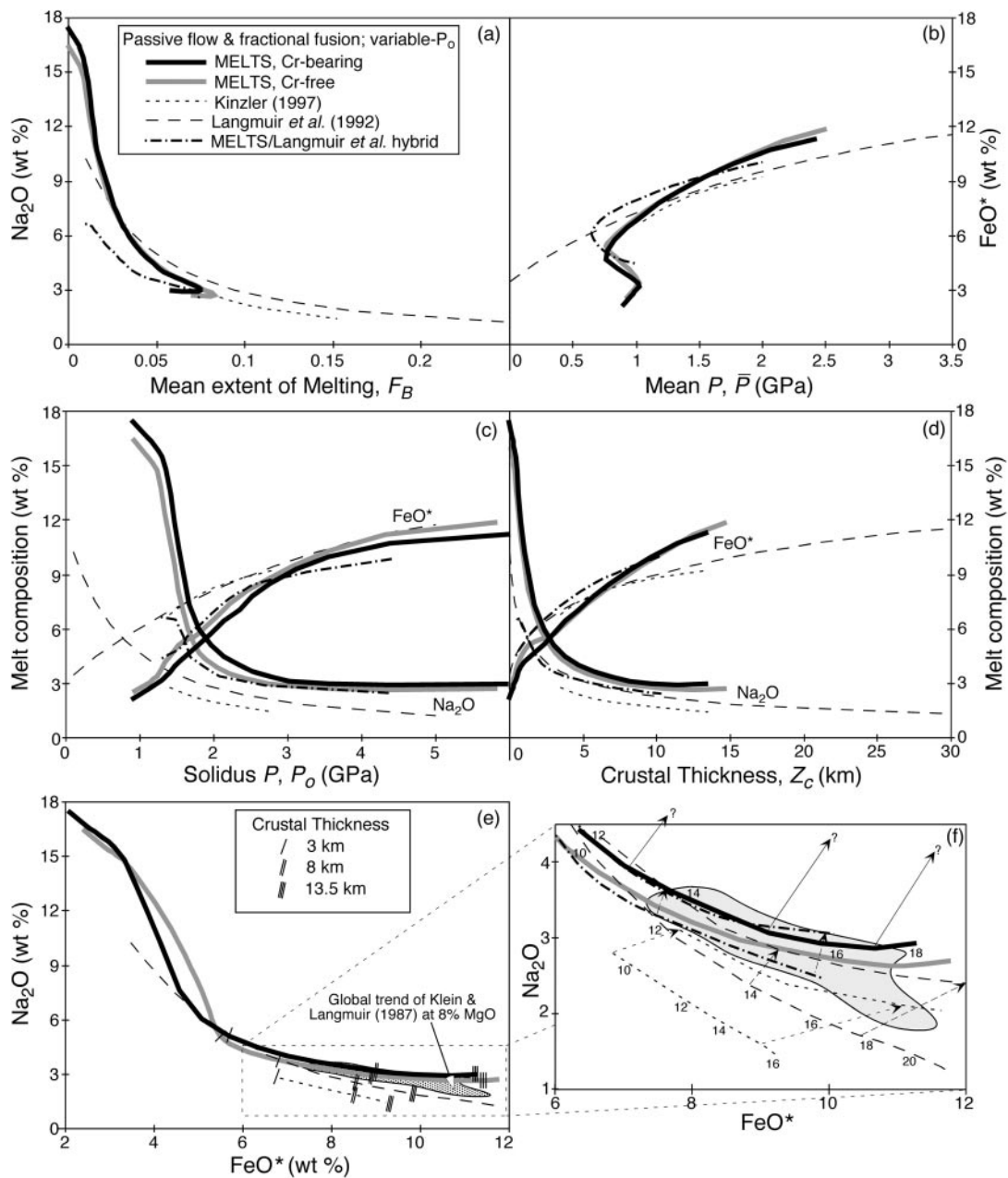


Fig. 7.

below and to the left of both of the pure model curves. The hybrid model retains the maximum in F_B and hence the minimum Na_2O feature of the pure MELTS model. The maximum Na_2O (i.e. at low F_B) is lower than the maximum from the pure Langmuir *et al.* model as a result of the temperature dependence of cpx D_{Na} in the Langmuir *et al.* model and the lower temperature in the MELTS model. The conclusions of this exercise are: (1) the functional relationship between primary aggregate liquid Na_2O and F_B depends on both the chemistry function and the melting function if these are viewed as separable; (2) the melting function predicted by MELTS tends to lower F_B at equal Na whereas the liquid chemistry in MELTS tends to raise Na at equal F_B relative to the Langmuir *et al.* model; (3) the direct error caused by high liquid Na_2O contents in MELTS dominates only below $F_B \sim 0.025$; (4) regardless of the chemical model, primary aggregate liquids with $\text{Na}_2\text{O} \leq 2.5\%$ require higher F_B than can result from perfect integration of passive-flow fractional melting regimes with the MELTS solidus and productivity function. A reliable Na_2O vs F_B model curve, however, will be available in the future only from a complete self-consistent model with accurate Na partitioning behavior.

FeO^* in aggregate liquids is sensitive to the mean pressure of melting, as emphasized by Langmuir & Hanson (1980) and Klein & Langmuir (1987). Figure 7b shows that for $\text{FeO}^* > 5\%$, the MELTS-calculated relationship between FeO^* and \bar{P} is similar to those calculated by the Langmuir *et al.* (1992) and Kinzler (1997) models, although the slope of the relationship predicted by MELTS is somewhat steeper. The detailed form of the FeO^* vs \bar{P} curves depends both on the liquid compositions predicted at particular P and F by each model and also on the productivity and P - T paths inherent in the models. At potential temperatures high enough to avoid the spinel-plagioclase transition, the similar slopes of the Langmuir *et al.* (1992) model and the hybrid calculation

imply that the overall slope of the aggregate FeO^* - \bar{P} curve depends mostly on the inherent pressure dependence of the chemistry functions. The absolute value of FeO^* at equal P , however, can be higher in the hybrid calculation than in either pure model. This is a complex result involving at least the effect of the P - T path (low productivity at low F gives a hotter path) and the effect of Na on Fe partitioning. As for Na_2O vs F_B , quantitative prediction of the FeO^* - \bar{P} curve will depend on future development of an accurate and self-consistent model where solidus temperature, productivity, melt chemistry, and the feedbacks between them are all correct.

At low P_0 and low FeO^* , MELTS predicts a significant change in the form of the FeO^* - P curve as a result of the energetic effect of the spinel-plagioclase transition. In the region where mean pressure is not monotonic with decreasing P_0 (see Fig. 5d), FeO^* continues to decrease smoothly with decreasing P_0 (Fig. 7c). The resulting reversal in the FeO^* - \bar{P} curve (Fig. 7b) reflects the productivity structure rather than the chemistry function; this is confirmed by its presence in hybrid calculations combining F - P - T relations from MELTS with Langmuir *et al.* (1992) chemistry. It should be noted that for any P_0 up to ~ 3 GPa, FeO^* in the incremental liquids from all the available chemical models is an increasing function both of pressure and extent of melting [see, e.g. Fig. 14e below and fig. 45 of Langmuir *et al.* (1992)]. The effects of decreasing pressure and increasing melt fraction during upwelling largely cancel each other, so from the solidus until cpx-out, changes in FeO^* with progressive upwelling and melting are predicted to be small [e.g. Fig. 14c below and fig. 48 of Langmuir *et al.* (1992)]. Consequently, FeO^* in aggregated liquids is predicted to be a more reliable indicator of the pressure of initiation of melting than of the mean pressure in regions where the relationship between these latter two variables is not monotonic. Although FeO^* in aggregate liquids has been interpreted primarily as an indicator of

Fig. 7. (*opposite*) Na_2O and FeO^* systematics for primary aggregate liquids in the case of passive flow and variable- P_0 global systematics for the Hart & Zindler (1986) source composition. In (a)–(e) these quantities are not fractionated to 8% MgO. The models of Langmuir *et al.* (1992) and Kinzler (1997) for polybaric fractional melting are shown for comparison. All curve patterns as in Fig. 5, except the dot-dashed curves, which show a hybrid model that applies the Langmuir *et al.* (1992) chemistry function along the F - T - P paths predicted by MELTS. (a) Na_2O vs F_B . (b) FeO^* vs mean P , \bar{P} . (c) Na_2O and FeO^* vs P_0 . (d) Na_2O and FeO^* vs crustal thickness. (e) Na_2O vs FeO^* . Tick marks indicate where along each curve the models generate crust of 3, 8, and 13.5 km thickness; the field of the global trend of fractionation-corrected regional averages from Klein & Langmuir (1987) is shown by the stippled field. (f) Enlargement of that part of the Na_2O - FeO^* plane most relevant to MORBs; the numbers along the primary liquid curves show weight percent MgO in the primary aggregate liquids. This plot also shows compositions fractionated to 8% MgO for comparison with the MORB data field. The calculation was performed using the program of Weaver & Langmuir (1990), modified to account for an average natural MORB water content of 0.25% (Reynolds, 1995). Fractional crystallization was calculated isobarically at 50 MPa in 1° temperature steps beginning at the liquidus. For the Langmuir *et al.* (1992) model primary liquids, which do not include predictions of CaO and Al_2O_3 contents, we inferred these oxides from the MgO contents of the primary liquids using fits to the Kinzler (1997) primary aggregate liquids for the same source. The fits are CaO (wt %) = $6 \times 10^{-6} \text{MgO}^3 - 0.0181 \text{MgO}^2 + 0.5602 \text{MgO} + 7.538$ (MgO in wt %, $r^2 = 1$, $n = 8$) and Al_2O_3 (wt %) = $24.175 e^{(-0.0306 \text{MgO})}$ ($r^2 = 0.9996$, $n = 8$). The family of evolved liquids resulting from various potential temperatures is shown for the Langmuir *et al.*, Kinzler, and hybrid models with the same dash-dot pattern as the primary liquids. Arrows connect parental and evolved liquids, but do not show the fractionation path between them. We attempted a fractionation calculation for the Cr-bearing MELTS results; these arrows are shown with question marks because they are outside the calibrated range of the fractionation program and in any case do not evolve along tholeiitic paths, as a result of artificially low SiO_2 and high Na_2O contents.

mean pressure (Klein & Langmuir, 1987), mean pressure has always been used in the past as a monotonic proxy for potential temperature; the current results suggest that this interpretation of FeO* in aggregated liquids in terms of T_P is sound even when the intermediate proxy of \bar{P} is complex.

When FeO* or Na₂O of the aggregate primary liquids are plotted against solidus pressure (Fig. 7c) the results of MELTS differ from previous models because of differences in the FeO*– P (Fig. 7b), Na₂O– F_B (Fig. 7a), and F_B – \bar{P} – P_o relations (Fig. 5). In particular, the low productivity of melting near the solidus predicted by MELTS results in F_B and P that are always lower than in the Langmuir *et al.* (1992) model for a given P_o . Consequently, for a given solidus pressure P_o , MELTS always predicts higher Na₂O and equal or lower FeO* in the aggregate melt from a 2D passive flow melting regime than previous models. This effect (for both Na₂O and FeO*) can be confidently attributed to the productivity structure of MELTS rather than to errors in partition coefficients because the offset is mostly preserved in hybrid calculations using Langmuir *et al.* chemistry and MELTS productivity (Fig. 7c). Furthermore, Na₂O in aggregate liquids predicted by MELTS is actually lower at equal F_B than that predicted by Langmuir *et al.* (1992) (Fig. 7a) for $0.025 < F_B < 0.08$. Although the higher P_o required by MELTS for a given aggregate Na₂O content compared with the Langmuir *et al.* (1992) predictions (Fig. 7c) can be explained by the differences in productivity, this result is not in fact independent of the Na-partitioning error in MELTS, as the self-consistent productivity prediction of MELTS is itself strongly affected by the liquid Na₂O contents (Hirschmann *et al.*, 1999a).

In principle, P_o can be observed directly by detailed seismic studies (e.g. MELT Seismic Team, 1998) and compared with MORB chemistry to test the predictions of various models shown in Fig. 7c. In the MELT region at 18°S on the East Pacific Rise, Fe₈ is 9.5–10.5% (Niu *et al.*, 1996). Hence (assuming the fractionation correction to be small) this is a ridge segment where the MELTS, Langmuir *et al.* and Kinzler models agree that the dry solidus should be at ~ 3 GPa (Fig. 7c). However, seismic evidence indicates a much deeper solidus (i.e. 6 GPa; MELT Seismic Team, 1998). The reason for this discrepancy is not known. It could be that Fig. 7 was constructed with incorrect assumptions about the mantle source composition, but on the basis of the discussion of the effect of heterogeneity on liquid FeO* given below, it would be difficult to account for all of this discrepancy in this way. More likely, the deep melting detected in the MELT region is an extremely low productivity deep melting ‘tail’ resulting from small amounts of a hydrous component (Hirth & Kohlstedt, 1996; Karato & Jung, 1998; Hirschmann *et al.*, 1999a). Accounting for the effects of H₂O remains an essential next step in the

development of accurate models for mid-ocean ridges generally, but quantitative modeling of hydrous melting at the required level of accuracy is not currently possible.

Primary aggregate liquid FeO* and Na₂O contents are plotted against crustal thickness in Fig. 7d. Above 5% FeO*, the plot of FeO* vs crustal thickness (Fig. 7d) is similar to that of FeO* vs P (Fig. 7b), as \bar{P} and crustal thickness scale similarly in MELTS and in constant productivity models (see Fig. 5a and c) at T_P high enough to avoid residual plagioclase. The plot of primary aggregate Na₂O against crustal thickness (Fig. 7d) shows again that MELTS predicts Na₂O uniformly higher than the Kinzler (1997) and Langmuir *et al.* (1992) models. Contrary to the equal- P_o comparison (Fig. 7c), however, the difference shown in Fig. 7d is attributable almost entirely to the errors in liquid Na₂O contents from MELTS. This is demonstrated by the hybrid calculations using the chemistry function of Langmuir *et al.* (1992) and the productivity function of MELTS, which yield Na₂O vs crustal thickness curves close to the unmodified Langmuir *et al.* curve in Fig. 7d. For simple passive-flow mixing models, crustal thickness is proportional to the product of F_B and P_T – P_o (Plank *et al.*, 1995). In the models shown here, the low F_B at given Na₂O (Fig. 7a) and the high P_o at given Na₂O (Fig. 7c) that result from the MELTS productivity function compared with the linear model effectively cancel, resulting in model Na₂O vs crustal thickness curves in Fig. 7d in which the differences reflect primarily the model chemistry functions.

Despite significant uncertainties in the interpretation of seismic and gravity-based crustal thickness measurements (Coulton *et al.*, 1995; Muller *et al.*, 1997), crustal thickness is more readily measured than P_o , so testing of the predictions shown in Fig. 7d should be easier than those of Fig. 7c. An important result of such a comparison is that even though the MELTS predictions are offset to high Na compared with the global dataset of regional averages of Na₈ and crustal thickness compiled by Klein & Langmuir (1987, fig. 14) and Forsyth (1992, fig. 52), the stronger curvature of the MELTS-predicted trend is mirrored by the available data (see Fig. 9d below). In particular, a highly curved trend of Na₈ vs crustal thickness such as MELTS predicts is required if all the data from Iceland to the Cayman Trough are to be explained with constant source and mixing geometry. In other words, in the absence of an enriched source, relatively low values of F_B at high values of crustal thickness are needed to explain chemical (Forsyth, 1992) and seismic velocity (Korenaga *et al.*, 2000) data from Iceland. This could result either from a large low-productivity region as in the passive-flow MELTS calculation or alternatively from focused flow at depth capped by a thick rheological boundary layer (Ito *et al.*, 1999).

In Fig. 7e and f, Na₂O is plotted against FeO* for primary aggregate liquids. Figure 7e shows the full range

of aggregate liquids generated across all potential temperatures; Fig. 7f blows up the range where actual regionally averaged MORB data plot when fractionated backwards or forwards to 8.0% MgO (Langmuir *et al.*, 1992). Comparing primary aggregate liquids, the predictions of the Langmuir *et al.* (1992) and MELTS models are generally similar for FeO* in the range 3–7%. In detail, however, as MELTS predicts a lower slope for Na₂O and a steeper slope for FeO* against crustal thickness (Fig. 7d) in the normal MORB range (i.e. crustal thickness between 5 and 8 km), the Na₂O vs FeO* trend from MELTS is more shallowly sloped than the predictions of Langmuir *et al.* (1992) or Kinzler (1997) above 7% FeO*. Above 10% FeO*, MELTS yields primary aggregate liquid Na₂O contents at least 1% higher than the other models at the same FeO*.

Figure 7f shows an attempt to calculate low-pressure fractional crystallization paths that bring the primary aggregate model liquids down to 8% using the fractionation engine of Weaver & Langmuir (1990) as updated by Reynolds (1995) (see the caption for details). The fractionation paths of the MELTS liquids are shown with question marks because these compositions are outside the calibrated range of the fractionation calculation. After fractionation, both the Langmuir *et al.* (1992) and Kinzler (1997) models match certain aspects of the global trend of MORB data at 8% MgO reasonably well. The current MELTS model does not match the data, owing chiefly to the high Na₂O contents of primary aggregate liquids that persist in the passive-flow MELTS model to high T_p and P_o . However, the hybrid model behaves well in fractionation calculations and falls within the range of the global trend data up to ~10% FeO*, indicating that the failure of MELTS to match the slope and position of the global trend is mostly attributable directly to the chemistry function. The hybrid model has a minimum primary liquid Na₂O content of 2.7% and so cannot match the high-Fe₈, low-Na₈ part of the MORB trend. As discussed above (Figs 4c, 5b and 7a), this minimum in Na reflects the curvature of the solidus and the low-productivity tail, which combine to produce a limit on F_B at high potential temperature for models with the MELTS productivity structure that collect all melts from the melting regime. Nevertheless, thick regions of ridge crust are observed to have Na₈ as low as 1.8%. If this result is robust, then either the simple mixing function used here is inappropriate for actual sub-ridge environments, some or all MORB source regions have a source more depleted in Na₂O than that used in the present calculations (0.3% Na₂O; see Fig. 10 below), or solidi or productivity functions (or both) like those of Langmuir *et al.* (1992), Kinzler (1997) or McKenzie & Bickle (1988) are more accurate than those predicted by MELTS. Although the concave-downward solidus and low near-solidus productivity are robust and reasonable

predictions of MELTS (Asimow *et al.*, 1997), their magnitudes are exaggerated in the current MELTS calibration by the effects of Na partitioning and poor constraints on the liquid model beyond ~3 GPa. A better understanding of thick, low-Na crustal segments will come from further seismic experiments defining the depth of the onset of melting and improvements to the melting models (particularly at the high pressures required by the MELTS productivity structure to generate normal oceanic crust). Nevertheless, the conclusion to be drawn from Fig. 7f is that if the productivity structure of adiabatic upwelling and the curvature of the solidus are even broadly similar to those predicted by MELTS, then the global trend of regionally average MORB compositions for crustal thickness above ~8 km defined by Klein & Langmuir (1987) is inconsistent with the standard mixing model of perfect aggregation from passive-flow melting regimes.

Passive flow, variable P_f

The global Na₂O–FeO* systematics resulting from integration of MELTS and Langmuir *et al.* (1992) liquids in variable- P_f melting regimes with globally constant initial pressure of melting is shown in Fig. 8. Na₂O increases with increasing P_f as a result of the corresponding decrease in F_B (Fig. 6). The increase is much larger in the MELTS output (except for the special case of $P_o = 1.3$ GPa, where all the melting is restricted to the region near P_o in MELTS), because of the overall lower values of F_B (see Fig. 7a). FeO*, on the other hand, is roughly constant as a function of P_f (except for $P_o = 4.4$ GPa) in the MELTS output, but systematically decreases with increasing P_f according to the Langmuir *et al.* (1992) chemistry and productivity functions (again, except for $P_o = 4.4$ GPa at low P_f). In both models, FeO* of instantaneous fractional melts increases with F at constant P and decreases with P at constant F , so the behavior of FeO* during polybaric melting depends on the productivity, $-dF/dP$. For roughly constant productivity, the increase in FeO* with F is the dominant behavior, such that FeO* increases with decreasing pressure through the melting regime at fixed potential temperature [Fig. 8b; this result was not anticipated by Klein & Langmuir (1989), who expected a positive correlation between FeO* and Na₂O among incremental liquids from within a given melting regime]. However, with the lower productivity predicted by MELTS at low F , the decrease in FeO* with P nearly balances the increase in FeO* with F , giving approximately constant FeO* throughout a melting regime of given potential temperature. However, although they differ in detail, the basic results of both models are the same: the Na₂O vs FeO* trends in

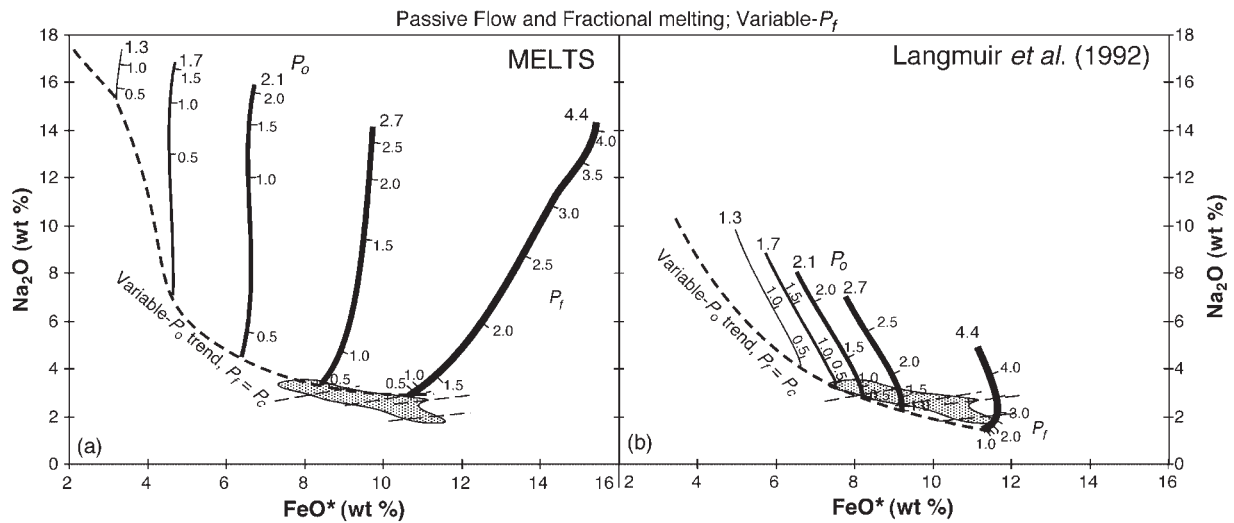


Fig. 8. Compositional trends in primary aggregate Na_2O and FeO^* predicted for variable- P_f melting regimes with passive flow and uniform HZ source composition according to (a) MELTS and (b) Langmuir *et al.* (1992). The same five potential temperatures are plotted as in Figs 4 and 6, although the intent is to evaluate how calculated global systematics vary with P_f at constant T_p . Each continuous curve shows tick marks at intervals of 0.5 GPa in P_f . The heavy dashed curve indicates the global trend as a result of variable- P_o systematics with P_f equal to the base of the crust at each T_p (see Fig. 7e). The stippled field in each panel shows the global MORB trend of Klein & Langmuir (1987) and the light long-dashed lines show typical slow-spreading local trends of Klein & Langmuir (1989), both at 8% MgO.

primary aggregate liquids generated by variations in P_f for a homogeneous mantle source and any constant potential temperature resemble neither the global trend (stippled fields in Fig. 8) nor local trends (light dashed lines in Fig. 8) of fractionation-corrected MORB data. Clearly, however, coupled variations in P_f and P_o would allow aggregate melt compositions to map out arbitrary fields in Na-Fe space, and such coupled variations could play a role (together with source heterogeneity, variations in mixing functions from segment to segment, variations in pressure of fractionation, etc.) in controlling the width of the MORB data field.

Active flow

The results shown in Figs 4–8 use the end-member passive-flow mixing model. An alternative simple model that has been considered is end-member active flow, in which all solid streamlines that cross the solidus are considered to pass through P_f and then descend, outside the melting regime, to fill the space of the residual mantle column (Forsyth, 1992; Langmuir *et al.*, 1992; Plank *et al.*, 1995; Shen & Forsyth, 1995). Active flow is usually envisioned to be the style of upwelling and melting associated with idealized plumes (e.g. Watson & McKenzie, 1991) and therefore is of greatest interest to ridge-related problems in regions that are plume affected, but some have argued that active flow may be also of quantitative importance more generally beneath ridges (Scott & Stevenson, 1989; Forsyth, 1992; Shen & Forsyth, 1995; Salters, 1996).

In active flow, the entire residual mantle column is characterized by an equal extent of depletion, F_{\max} ; in this case, F_B is equal to F_{\max} (Plank *et al.*, 1995). If the thickness of the residual mantle column is defined by P_o (Langmuir *et al.*, 1992; Plank *et al.*, 1995), then crustal thickness (and hence P_f if cooling is not imposed at greater depth) is determined by $P_c = F_{\max}(P_o - P_c)$. Clearly, the physical requirements on mantle flow implied by this mixing model (much like the melt flow implied by perfect aggregation of melts from passive-flow regimes), become more extreme with increasing P_o , as the flux of mantle through the melting regime and magnitude of the down-flow outside the melting regime must also increase.

Figure 9 shows selected results of active-flow melting regimes using MELTS and the model of Langmuir *et al.* (1992). For a given melting model, active flow produces thicker crust at equal P_o or T_p than passive flow. The shapes of the crustal thickness curves plotted against P_o (Fig. 9a), however, remain similar: the MELTS results are still concave down and the Langmuir *et al.* (1992) results are still concave up (ζ_c being roughly proportional to P_o^2 for roughly constant productivity whether active or passive). As crustal thickness in an end-member active flow regime is given by $F_{\max}(P_o - P_c)$, when plotted against P_o the differences between models are entirely attributable to differences in F_{\max} . As we have seen (Fig. 4), the Langmuir *et al.* (1992) model is based on near-constant productivity for lherzolite melting (except for a pressure correction of 1 part in 88 per kilobar) and a 20% lower productivity for harzburgite. The break in slope between the two parabolic sections of the Langmuir *et al.* (1992)

active melting curve (that is, where F_{\max} becomes greater than cpx-out) is hardly visible in Fig. 9a. The MELTS curve, on the other hand, has three clearly distinguishable sections: a low-slope segment up to $P_o = 1.3$ GPa controlled by the spinel–plagioclase transition, where the entire melting regime is in the low-productivity tail; a steep segment up to $P_o = 2.1$ GPa, where F_{\max} is in the high-productivity melting regime between $F \sim 0.03$ and cpx-out; and an intermediate slope segment beyond $P_o = 2.1$ GPa where F_{\max} is within the relatively low-productivity harzburgite-melting regime (and, furthermore, average productivity throughout the melting regime continues to drop with increasing P_o ; see Fig. 4a). Despite the different shapes of the curves, however, it is clear that active flow can readily generate at least 35 km thick crust (comparable with central Iceland; Menke, 1999), even with the limits imposed by MELTS.

The means by which MELTS can generate up to 35 km of crust by active flow can be understood from Fig. 9b, where the MELTS-calculated curve of crustal thickness vs T_p becomes nearly vertical as T_p approaches 1500°C. As noted above (e.g. Figs 1a and 2), according to MELTS the solidus of fertile peridotite becomes tangent to the subsolidus adiabat at $P_o \sim 6.4$ GPa and $T_p \sim 1500^\circ\text{C}$. As the active-flow formalism has crustal thickness proportional to $F_{\max}(P_o - P_c)$, crustal thickness also approaches a vertical tangent and would jump to ~ 100 km if we were to attempt to apply this formalism beyond $T_p = 1500^\circ\text{C}$ (because then P_o would jump discontinuously to ~ 13.8 GPa, i.e. the 410 km seismic discontinuity, where the solidus kinks sharply upwards). Although these details are dependent on the essentially unconstrained high-pressure extrapolation of MELTS, the strict active-flow formalism requires a solid streamline to descend all the way from P_c to P_o outside the melting regime, and as P_o increases rapidly, the mass flux through the melting regime implied by this flow field increases in proportion: that is, when $P_o = 6$ GPa, this formalism implies that all the solid mantle constituting an ~ 180 km thick residual mantle column has been funneled through an ~ 10 km wide melting column and then descended to its final location from $P_c \sim 1$ GPa. As indicated above, although plausible perhaps as a process for low values of P_o , this becomes increasingly unrealistic with increasing solidus depth.

The compositional implications of active flow are summarized in Fig. 9c and d, where primary aggregate Na_2O is plotted against FeO^* and against crustal thickness. Na_8 and Fe_8 are also shown in Fig. 9c, with the MELTS results uncertain as they are outside the calibrated range of the fractionation calculation. The active-flow trend in Na_2O vs FeO^* predicted by the Langmuir *et al.* (1992) model is roughly parallel to the passive-flow trend, but offset to lower Na and Fe, as F_B is higher and \bar{P} is lower. In contrast, the active-flow MELTS calculation yields a

flatter trend than the passive-flow MELTS calculation, and there is a larger offset between the two mixing models than in the Langmuir *et al.* (1992) results. The larger offset between mixing models in the MELTS calculations is attributable to the steeper FeO^* vs \bar{P} trend output by MELTS (Fig. 7b) and to the larger difference in F_B between mixing models as a result of the productivity variations in MELTS. With the Langmuir *et al.* productivity structure, the ratio of F_{\max} to passive F_B is always ~ 1.75 . In MELTS this ratio may be as large as 3.7 as a result of the weighting of the large low-productivity regime in the passive-flow calculation. The low slope of the active-flow Na_2O vs FeO^* trend calculated by MELTS that is so prominent in Fig. 9c above $\text{FeO}^* = 6\%$ results from causes similar to those underlying the corresponding passive-flow trend (Fig. 7f): i.e. FeO^* and P increase with P_o , for a 1D average much like the 2D average for passive flow; Na_2O , on the other hand, becomes flat in the active-flow results because F_{\max} , like F_B , increases slowly at high P_o (see Fig. 4c). In the case that F_{\max} occurs at the base of the crust, the rapid increase in active-flow P_c at high P_o (Fig. 9a) actually leads to a maximum in F_{\max} and a corresponding minimum in Na_2O from active-flow regimes. The hybrid calculation for active flow gives a Na_2O – FeO^* curve similar to the pure Langmuir result except above $\sim 8\%$ FeO^* , where the approach to the maximum in F_{\max} in the MELTS productivity structure takes over and the hybrid curve, even for active flow, fails to reach the low Na_2O and Na_8 values required by the shallowest ridge segments.

Although, on the basis of Figs 7f and 9c, neither the active-flow nor the passive-flow trends predicted by MELTS seem likely to fractionate to a steep enough trend to fit the global Na_8 vs Fe_8 trend defined by MORB (Klein & Langmuir, 1987), an intriguing and not unreasonable possibility is a systematic correlation between the importance of active flow and potential temperature. If high potential temperature is systematically associated with mantle plumes, or if the importance of internal buoyancy in the melting regime increases with T_p (as a result of lower matrix viscosity, greater compositional buoyancy of depleted residues, or higher retained melt fractions), it is possible that the observed global trend is due to mixed active and passive flow regimes such that the low- T_p end of the passive-flow model connects to the high- T_p end of the active-flow model. In this case, the observed global trend of Klein & Langmuir (1987) might well be consistent with the productivity structure predicted by the MELTS model.

Figure 9d shows that, using the Langmuir *et al.* (1992) chemistry and productivity models, active flow and passive flow generate roughly parallel trends in Na_2O vs crustal thickness, with active flow offset to Na_2O 0.2–0.3% lower at equal ζ . These parallel trends are contrary to

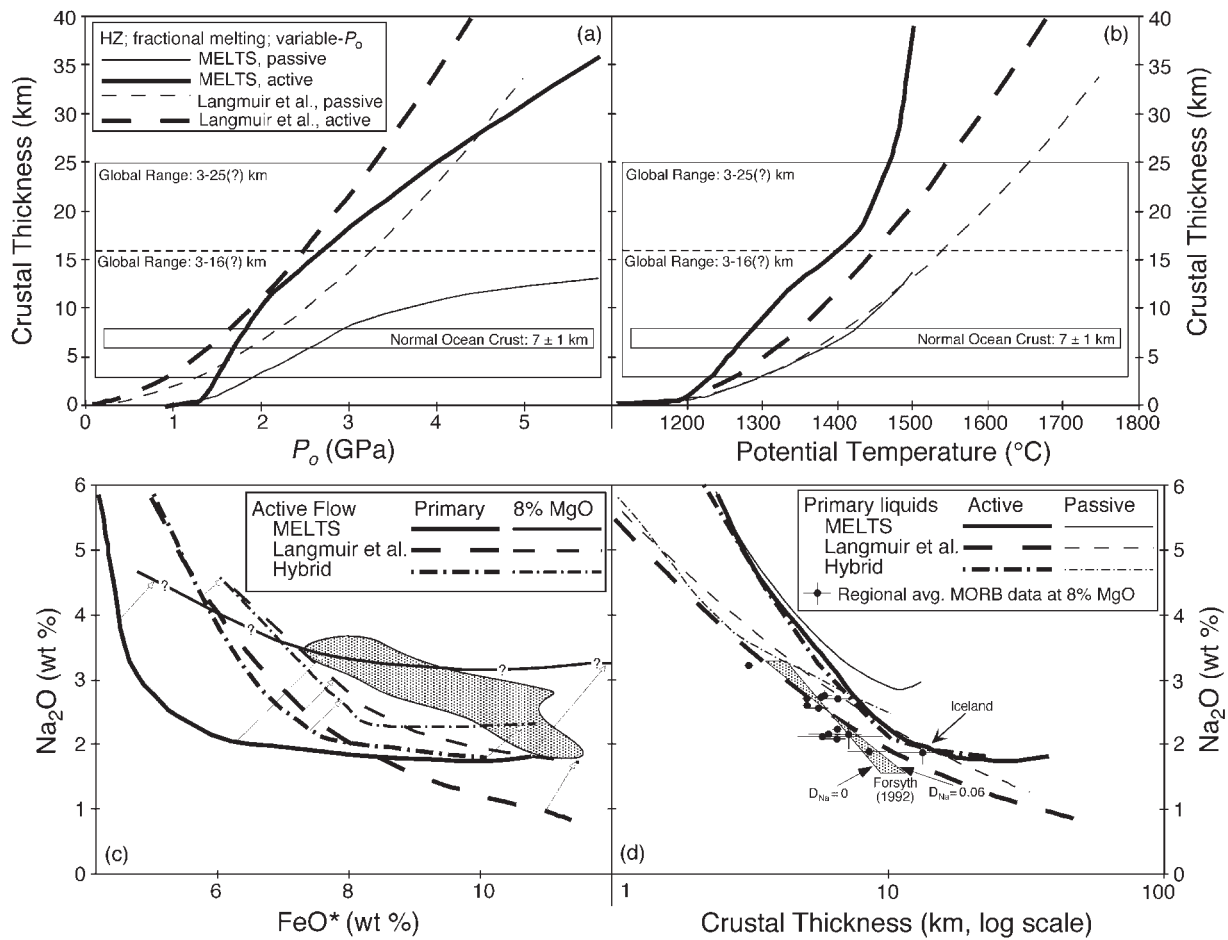


Fig. 9. Comparison of the end-member active-flow mixing models with the passive-flow calculations presented in Figs 5 and 7. Light curves are passive-flow results for the Cr-bearing Hart & Zindler (1986) source composition. Heavy curves show active-flow models. (a) Crustal thickness vs P_o (see text for discussion of the formalism for calculating crustal thickness for active flow). (b) Crustal thickness vs T_p . (c) Na_2O vs FeO^* in the primary aggregate liquid. The dot-dashed curve shows a hybrid calculation that applies the Langmuir *et al.* (1992) chemistry function along the MELTS-predicted P - T - F path. Fractionation to 8% MgO is shown for each model (as described in the caption to Fig. 7) with the same pattern and a lighter pen. The stippled field is the global trend of regional MORB averages at 8% MgO from Klein & Langmuir (1987). (d) Primary aggregate liquid Na_2O vs crustal thickness on a logarithmic scale. Also shown is the compilation of segment-average Na_8 vs crustal thickness and predictions of active-flow trends for D_{Na} between 0 and 0.06, both by Forsyth (1992).

the scaling argument given by Forsyth (1992), who argued that the global trend in Na_8 vs ζ_c (with the exception of the Iceland datum) is consistent with $\zeta_c \propto F_{\text{max}}$ (and $\text{Na}_8 \propto 1/F_{\text{max}}$) and associated this scaling with active flow. Figure 9a shows that the active-flow calculation based on Langmuir *et al.* (1992) retains $\zeta_c \propto F_{\text{max}}^2$. The scaling assumed by Forsyth can result only if the thickness of the residual mantle column is constant [let us call this constant depth P_r , so that $P_c = F_{\text{max}}(P_r - P_o)$], i.e. if active flow always generates a residual mantle column of equal height regardless of P_o . It is unclear in this case, however, what would be the fate of mantle that crosses P_o , but finally forms the far-field mantle column between P_o and P_r . Unless the axial region is hotter than surrounding mantle (i.e. as a result of a plume), this material should

melt, and strict active-flow mixing together with a constant thickness residual mantle column would require that these melts do not reach the axis.

The slope of the Na_8 vs log crustal thickness plot for most of the regionally averaged MORB data, as well as the Iceland point offset to higher crustal thickness or higher Na_8 than other data, are both broadly consistent with constant source composition if the form of the active-flow MELTS curve is correct (or with passive flow at most ridge segments and active flow at Iceland). It is difficult to interpret this result quantitatively at present because of the problems with Na in melting and fractionation calculations with MELTS, but in general the shape of this curve reflects the productivity structure and solidus shape (as demonstrated in Fig. 9d by the similarity

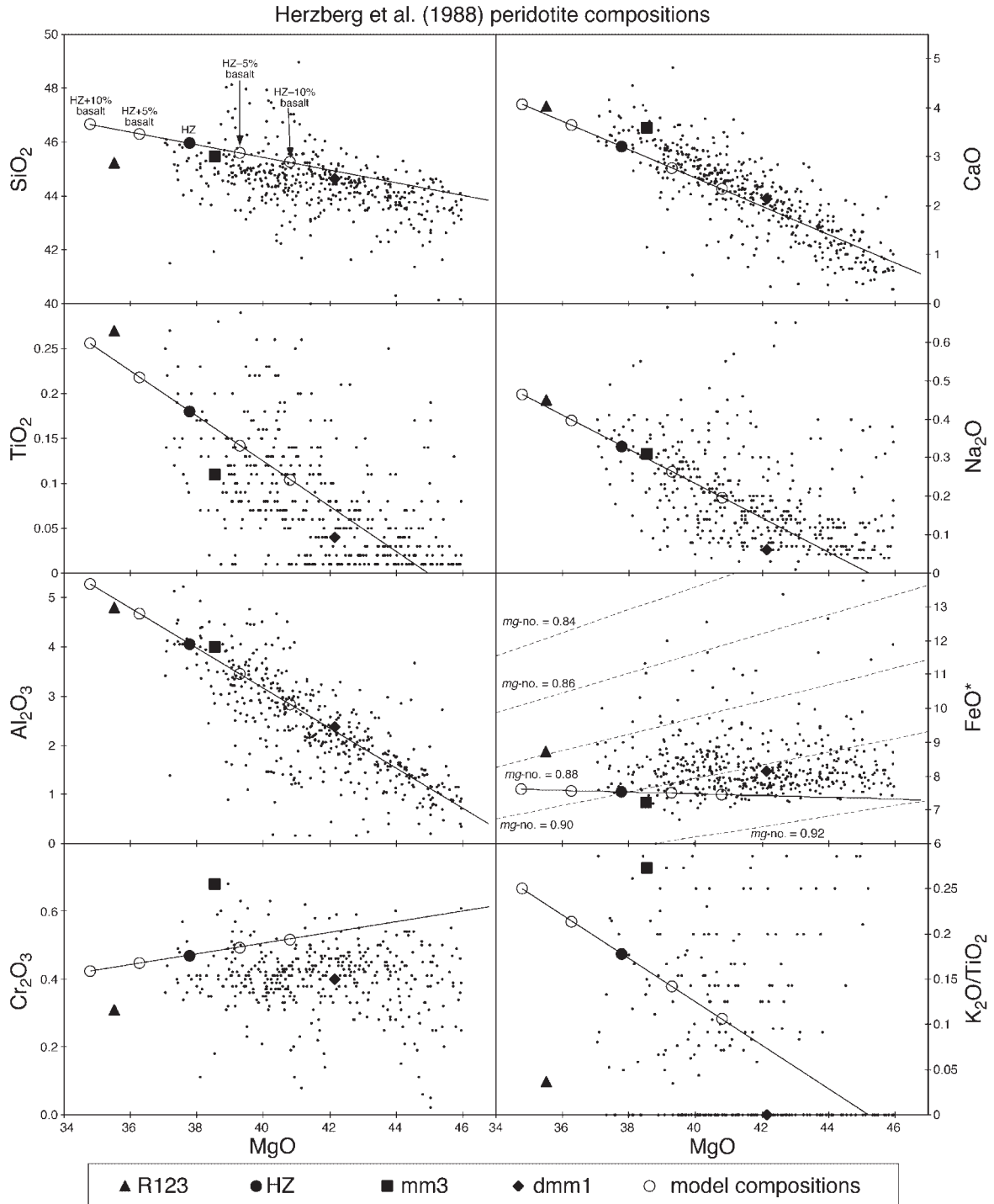


Fig. 10. Small points show compositions in a global sample of peridotites (Herzberg *et al.*, 1988). The lines represent addition and subtraction of a uniform basaltic component from the primitive upper mantle composition of Hart & Zindler (1986). This component (in wt %: SiO₂ 49.15; TiO₂ 1.49; Al₂O₃ 15.65; FeO* 10.27; MgO 7.44; CaO 11.44; Na₂O 2.57; K₂O, see text) was chosen so that the enrichment–depletion trend would parallel the principal trends of variation in the peridotite data. It is offset from the bulk of the data in those elements for which the starting composition is not in the center of the data array. The circles show the five compositions used in calculations of the effects of source heterogeneity, i.e. HZ + 10% basalt, HZ + 5% basalt, HZ (●), HZ – 5% basalt, and HZ – 10% basalt. ▲, enriched peridotite R123 (Frey *et al.*, 1985); ■, experimental mix mm3 representing a fertile peridotite (Baker & Stolper, 1994); ◆, experimental mix DMM1 representing a depleted peridotite (Wasylenki *et al.*, 1996).

between the MELTS result and the active-flow hybrid calculation). The key point is that active flow in a near-constant-productivity, linear-solidus model (e.g. Langmuir *et al.*, 1992) is not sufficient to explain the discrepancies between crustal thickness and melt chemistry (Forsyth, 1992) or crustal density at Iceland (Korenaga *et al.*, 2000). The MELTS model, with its large low-productivity region at high pressure at high potential temperature, can, however, produce the required effect, although quantitative details must await improved models. Although the pure active-flow mixing model used here requires an apparently rather unlikely mantle flow field, dynamical calculations (e.g. Ito *et al.*, 1999) indicate that a rheological boundary layer resulting from the effect of melt extraction on viscosity (Hirth & Kohlstedt, 1996) may lead to a similar mixing function.

EFFECTS OF SOURCE HETEROGENEITY

In principle, the ability to compute aggregate liquids from multiple source compositions is one of the most promising applications of MELTS to the study of variations in MORB compositions, as MELTS is not calibrated solely using melting experiments on any particular source composition. Opinions differ as to whether major element heterogeneity of the sources of MORBs constitutes a major contributor to the spectrum of variability in erupted liquids: for example, Langmuir *et al.* (1992) argued that such heterogeneity does not control the global trend of regionally averaged compositions or the local trends observed at slow-spreading ridges, but may explain the local trend on the fast-spreading East Pacific Rise and anomalous regions around some hotspots. This view is consistent with evidence of isotopic correlation with local variations on the EPR and the absence of such correlation on slow-spreading ridges (see Langmuir *et al.*, 1992). On the other hand, Shen & Forsyth (1995) maintained, on the basis of trends in K_2O/TiO_2 and $(Sm/Yb)_N$, that the global trend is mostly a manifestation of source heterogeneity (see also Zindler *et al.*, 1996). Niu & Hékinian (1997a, 1997b), although advocating a physical picture of ridge melting similar to that by Shen & Forsyth, dismissed the possibility that source heterogeneity controls major-element trends such as CaO/Al_2O_3 . Several of the effects of source heterogeneity on isobaric melting trends were modeled using MELTS by Hirschmann *et al.* (1999b). Here we extend this discussion to consider integrated melt compositions from isentropic or incrementally isentropic polybaric passive-flow and active-flow melting regimes and use these results as a guide to recognizing possible manifestations of source heterogeneity on MORB compositions.

The compositional range of natural peridotites (Herzberg *et al.*, 1988) is large and complex, and cannot be reduced to a single vector in composition space (Fig. 10). Nevertheless, for simplicity we have chosen a 1D array of source compositions to illustrate the effects of source variations along a trend from 'enriched' to 'depleted' peridotites. We chose a constant basaltic component to add or subtract from the Hart & Zindler (1986) primitive upper-mantle composition, generating the lines shown in Fig. 10, which, for most chemical indicators, either overlie or parallel the major trend of chemical variation in natural peridotites. In what follows we use five compositions along this line corresponding to the Hart & Zindler composition with 5% or 10% by mass of the basaltic component added or subtracted; the resulting five compositions are plotted in Fig. 10 for comparison with the field of observed peridotite compositions in the Herzberg database. Also shown are experimental mixes mm3 (Baker & Stolper, 1994) and DMM1 (Wasylenki *et al.*, 1996) and sample R123 (Frey *et al.*, 1985), a particularly enriched peridotite from the Ronda massif [see discussion of these compositions by Hirschmann *et al.* (1999b)].

Na_2O-FeO^*

The Na_2O-FeO^* systematics of aggregate primary liquids from the MELTS model is explored in the light of variable source composition in Figs 11 and 12. We begin with variable- P_f , constant- P_o systematics in Fig. 11 because in this view it is easier to monitor the progress of incremental or integrated composition with progressive melting. Using Fig. 12, we discuss (below) variations in aggregate composition caused by source heterogeneity from variable- P_o melting regimes. The outstanding questions concerning source heterogeneity and Na_2O-FeO^* systematics are the importance of regional source variations in determining the global trend of Klein & Langmuir (1987) and the importance of local source variations in generating local trends, either for slow-spreading ridges (low positive slopes; Brodholt & Batiza, 1989; Klein & Langmuir, 1989) or fast-spreading ridges (negative slopes sub-parallel to the global trend; Langmuir *et al.*, 1992).

Figure 11 presents Na_2O-FeO^* systematics for variable- P_f melting regimes with constant potential temperature ($1325^\circ C$; $P_o = 2.1$ GPa for the reference composition). Variations in P_f for each source composition and any integration model produce S-shaped curves with generally steep slopes. Most of these integrated trends owing to P_f variation do not correspond simply to any global or local systematics of MORBs for any constant composition or mixing model (note the expanded FeO^* scale in these plots compared with Fig. 8), although, as emphasized repeatedly, the precise shapes of these curves are inaccurate because of the low partition coefficient for Na in MELTS.

The lowest- P segments of the incremental fractional liquid paths (Fig. 11a) do resemble the slow-spreading local trends of Klein & Langmuir (1989). Comparison of local trend data with only part of the incremental liquid curve, however, implies that only increments of liquid from shallow depths (or mixtures thereof) are sampled, with no sampling or admixture of higher-pressure increments. This would require that the high-pressure increments do not erupt from the axis. The active-flow batch melting curves (Fig. 11d) also define trends similar to these local trends across a wide range of source compositions and potential temperatures (although only one T_p is shown in Fig. 11d). This is of limited interest because the active-flow batch melting model is inconsistent with evidence requiring MORB liquids to be isolated from residues in the shallow mantle (Kelemen *et al.*, 1997), with the simplest interpretation of abyssal peridotite data (Johnson *et al.*, 1990), and with the form of the melting region imaged in the MELT area of the East Pacific Rise (MELT Seismic Team, 1998).

Contours of constant P_f across heterogeneous source compositions are shown in Fig. 11 as light continuous curves. The shaded curves labeled $P_f = P_c$ show the particular case where melting stops at the base of the crust and are identical to the $T_p = 1325^\circ\text{C}$ curves in Fig. 12 below. The constant depth contours (i.e. heterogeneity vectors) in Fig. 11 can have slopes ranging from negative (for batch fusion with active flow, Fig. 11d) to positive and much steeper than typical slow-spreading local vectors [e.g. Fig. 11c; this is the slope predicted by Klein & Langmuir (1989)]. These positive and negative slopes are also found for isothermal curves connecting isobaric batch melting trends of various source compositions at 1 GPa (Hirschmann *et al.*, 1999b): at equal P and F , a more enriched source yields more Na in the liquid, but at equal P and T , enriched sources

yield higher F and so may give higher or lower liquid Na than more depleted sources. The counterintuitive behavior (higher Na in liquids from more depleted sources) is restricted to low temperatures for isobaric melting, with the expected behavior (Na content of isobaric batch melts increasing with source enrichment)

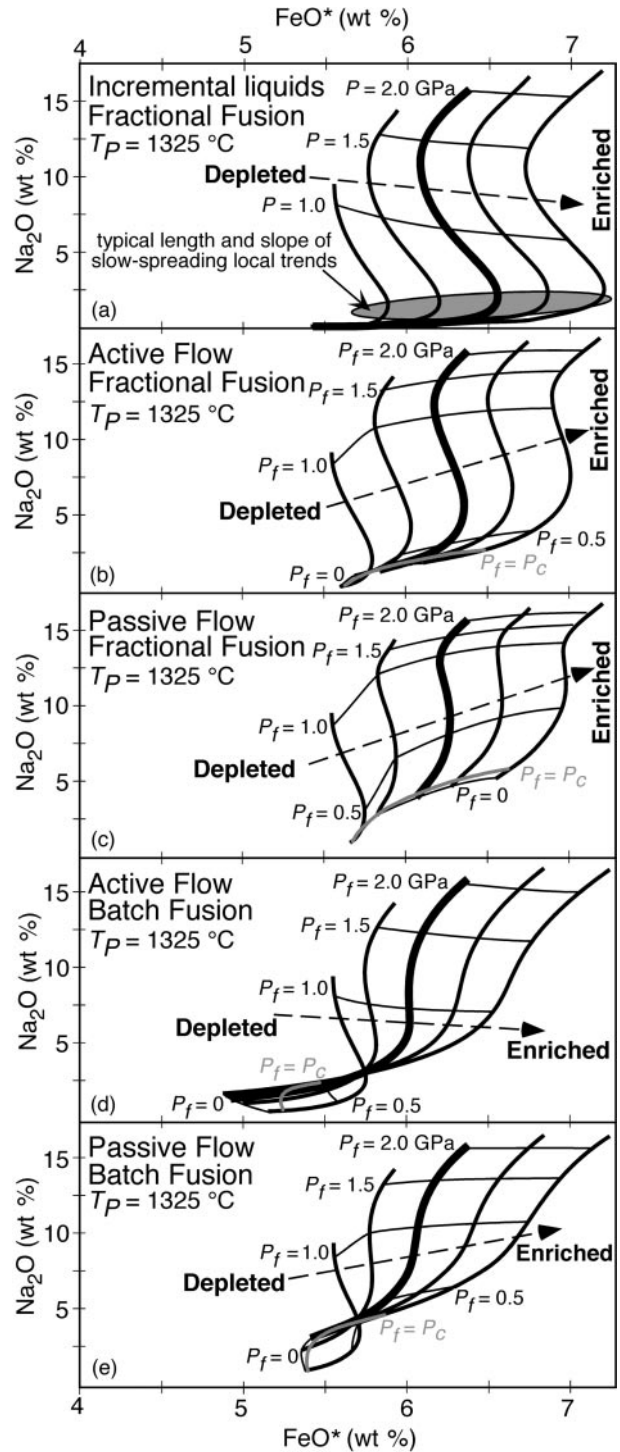


Fig. 11. Na_2O vs FeO^* for melting regimes with various source compositions (see Fig. 10) with constant potential temperature (1325°C) and varying final depth of melting, P_f : (a) incremental fractional melt compositions; (b) integrated compositions for active flow and fractional melting; (c) aggregate compositions for passive flow and fractional melting; (d) active flow and batch melting; (e) passive flow and batch melting. The bold S-shaped curves in each case show variation of P_f from P_o to zero for each source composition. The extra-bold curve in the center represents the Cr-bearing Hart & Zindler (1986) reference composition used in Figs 1–9; for (c) this curve is identical to the $P_o = 2.1$ GPa curve in Fig. 8a. The light, shallowly sloped curves show constant P_f contours for the various source compositions. The shaded curves labeled $P_f = P_c$ show the composition at the average base of the crust in each case, which is close to the $P_f = 0$ contour except for active flow cases with enriched sources, where the crust may reach thickness (in pressure units) up to 0.5 GPa. These shaded curves correspond exactly to the $T_p = 1325^\circ\text{C}$ contours in Fig. 12. The shaded elliptical field in (a) represents the typical length and slope of the slow-spreading local trends of Klein & Langmuir (1989), but its position is arbitrary.

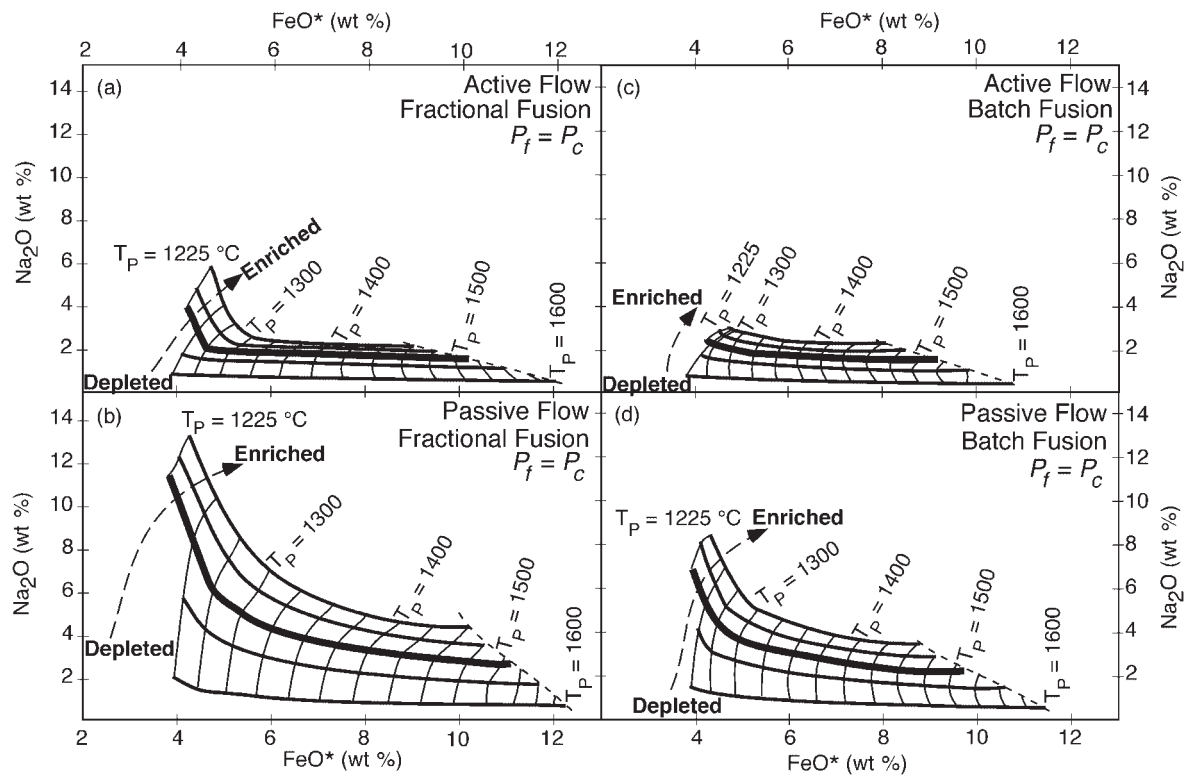


Fig. 12. Na_2O vs FeO^* for primary integrated liquid compositions for (a) active flow and fractional melting, (b) passive flow and fractional melting, (c) active flow and batch melting, and (d) passive flow and batch melting. All panels are for melting regimes with P_f set equal to the base of the crust, variable potential temperature (1225–1600°C), and five source compositions (see Fig. 10). The heavy curves with negative slopes are for each source and various potential temperatures [extra heavy for the Cr-bearing reference composition of Hart & Zindler (1986)]. The light curves are contours of constant potential temperature spanning the range of source composition. For this calculation, an arbitrary maximum depth of 6.5 GPa was placed on the base of the residual mantle column, close to the depth at which the solidus and adiabat cease to intersect for the HZ composition and the integration methods for aggregate melting regimes break down; the light dashed curve on the right of each figure shows this cutoff.

at equal T obtaining above $\sim 1300^\circ\text{C}$ at 1 GPa; the change in Na_2O vs F slope of the 1 GPa experimental or MELTS-calculated isotherms occurs at $\text{Na}_2\text{O} \sim 2$ wt %. In polybaric calculations, we observe decreasing Na with enrichment of the source at equal P for incremental fractional liquid compositions (Fig. 11a) or active-flow batch melts (Fig. 11d) only for $P > 0.6$ GPa. For the potential temperature shown in Fig. 11, the changes in sign of the isobar slopes occurring near $P = 0.6$ GPa for both batch and fractional melting correspond to $\text{Na}_2\text{O} \sim 2\%$ [visible in Fig. 11d (note the direction of the $P_f = 0.5$ GPa contour) but concealed by the incremental paths in Fig. 11a]. In fact, across the whole range of T_p from 1200 to 1600°C, the change in slope for incremental liquids always occurs near $\text{Na}_2\text{O} \sim 2\%$, although the P at which this occurs varies with T_p . Furthermore, the trend of decreasing Na with increasing enrichment disappears upon integration of liquids for either active flow or passive flow (i.e. Fig. 11b, c and e); i.e. the isobaric variation of liquid Na content in aggregate liquids always has the same sense as the source variations.

The constant- P_f , variable source composition contours in Fig. 11 allow us to evaluate whether the slow-spreading local trend of Klein & Langmuir (1989) could be related to source heterogeneity, given certain assumptions about mixing of liquids and P - T paths in heterogeneous melting regions, and acknowledging that there are no isotopic or trace-element data to support a role for heterogeneity in slow-spreading local trends (Langmuir *et al.*, 1992). We have seen that within melting regimes of constant potential temperature and homogeneous source composition (i.e. the S-shaped curves in Fig. 11 discussed so far), neither uniform sampling of incremental liquids nor complete mixing of liquids up to variable segregation pressures (except perhaps the extreme case of active flow with batch melting; Fig. 11d) can generate systematics like that observed at segment scale on slow-spreading ridges, either with the model of Langmuir *et al.* (1992) (Fig. 8) or with MELTS (Figs 8 and 11). The range of source heterogeneity considered here does, however, give a range in FeO^* values at constant P_f of up to 1.25%, which is comparable with the lengths of most

slow-spreading local trends. This FeO* range is similar to that given by Langmuir *et al.* (1992) for $P_f = P_c$ using a similar range of sources and their chemistry function. As the MELTS modeling also considers the effect of heterogeneity on productivity [discussed for isobaric

melting by Hirschmann *et al.* (1999a)], more quantitative statements can be made about the coupled range in Na₂O and the slope as a result of heterogeneity if Na values from MELTS were more accurate. At present, we can conclude only that the typical slopes of slow-spreading local vectors are within the range of allowable slopes as a result of heterogeneity for certain mixing models and P_f values.

Figure 12 shows Na₂O vs FeO* in primary aggregate melts for variable- P_o systematics (i.e. P_f equal to the base of the crust) with active and passive flow fields, batch and fractional melting, and five source compositions. With varying potential temperature, each composition generates a negative correlation as expected for global trend systematics. A comparison of the batch melting cases with the fractional cases confirms the general rule that fractional fusion generates a wider range of melt compositions than does batch melting (Presnall, 1969) and the more specific conclusion of Langmuir *et al.* (1992) that batch melting generates a smaller range of FeO* in integrated melts than fractional melting, although this difference is minor.

Klein & Langmuir (1987) and Langmuir *et al.* (1992) argued that source heterogeneity of the sort explored here will produce positive correlations between Na₂O and FeO* contents in integrated melts. This is supported by calculations of the Na₂O–FeO* trends produced by varying source composition at constant T_p , which have steep positive slopes for passive flow and fractional melting (Fig. 12b). For active flow and/or batch melting, however, at potential temperatures above 1350–1400°C the contours may show negative slopes for the depleted compositions as a result of melting beyond the exhaustion of cpx, where FeO* decreases strongly with increasing F . This signal is seen most strongly in those mixing models that strongly weight high- F liquids; i.e. no negative slopes are seen for passive flow plus fractional melting (i.e. Fig. 12c) even on those paths that exhaust cpx. It should be noted that decreasing FeO* with increasing source enrichment is more easily seen at constant P_f and T_p than at the base of the crust, as P_c at equal T_p increases

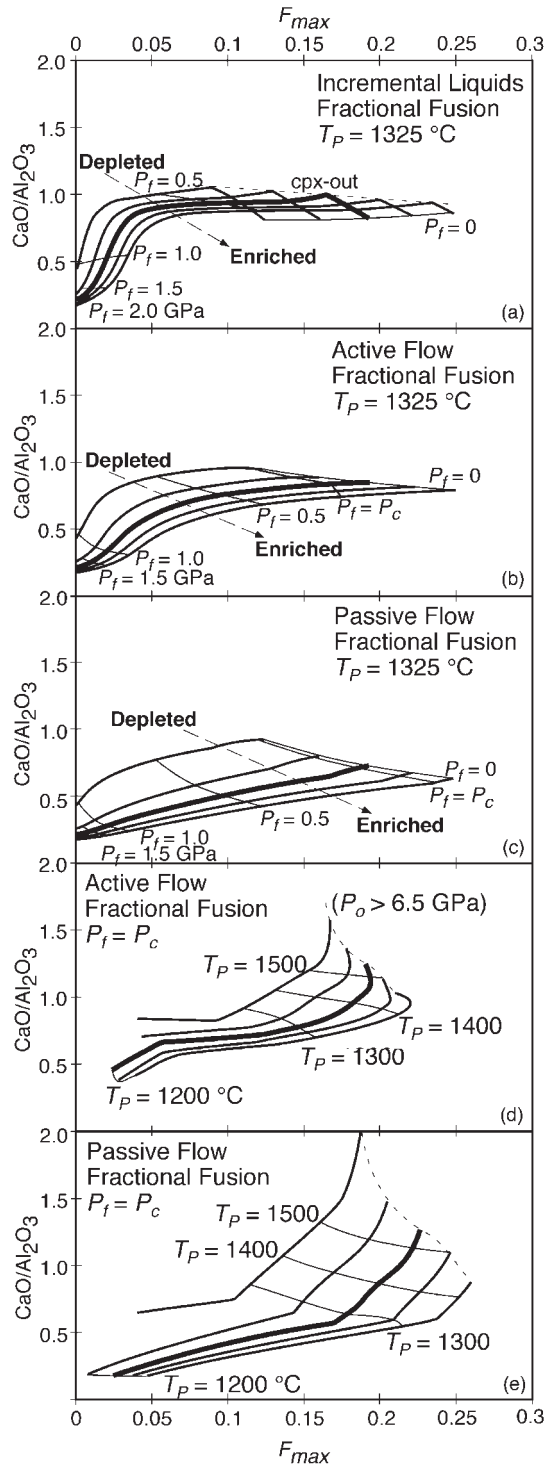


Fig. 13. CaO/Al₂O₃ in instantaneous or aggregate primary melt compositions vs maximum extent of melting for various sources (see Fig. 10) with a range of melting and mixing models. Constant source composition is indicated by heavy curves [extra heavy for Cr-bearing reference source of Hart & Zindler (1986)]. (a)–(c), variable- P_f melting regimes with potential temperature equal to 1325°C; light contours show equal pressure, either the pressure where (a) increments of melt or partial mixtures might be sampled or where [(b) and (c)] the output from the melting regime ceases (i.e. P_f). (d) and (e), variable- P_o melting regimes with melting and integration continuing always to the base of the crust; light contours show equal potential temperature. The curves in (d) and (e) are cut off on the right side at $P_o = 6.5$ GPa, as described for Fig. 12.

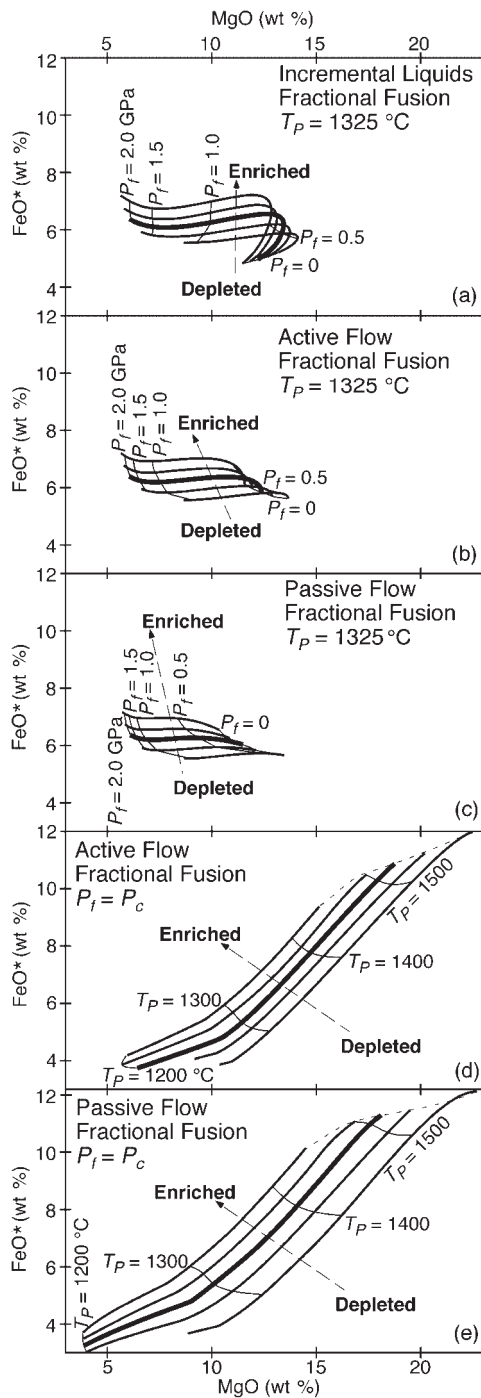


Fig. 14. FeO* vs MgO in primary melt compositions. Symbols and calculations as in Fig. 13. The dashed cutoffs at the tops of (d) and (e) are for $P_o = 6.5$ GPa, as for Fig. 12.

with increasing enrichment of the source (compare $P_f = 0$ and $P_f = P_c$ contours in Fig. 11d).

In no case do the constant T_p contours at the base of the crust in Fig. 12 correspond to the typical slopes of any local trends. Figure 11, however, showed that the

shape and slope of constant T_p , constant P_f contours vary strongly with mixing model and with P_f . Furthermore, the particular constant-depth contours in Fig. 11 represent very specific assumptions about the way increments of melt might mix to produce individual samples that define a local trend. Namely, these contours are calculated assuming that melts from peridotites of each composition are aggregated first, before mixing with melts from other source components. These calculations further assume that each source composition follows its own adiabatic path. In an adiabatic mantle that is isothermal below the solidus, once melting begins each source composition follows a distinct P - T path controlled by its local productivity. However, if there is any thermal interaction between the domains, the local melt production will be affected and the result will be different (Hirschmann & Stolper, 1996; Hirschmann *et al.*, 1999b).

A proper evaluation of the role of mixing and heterogeneities of various scale in local variation of MORB chemistry will require calculations beyond the scope of this paper that simultaneously consider melting, chemistry, and dynamics of two-phase flow in at least two dimensions as well as trace element and isotopic data in addition to major-element constraints. Although it is consequently difficult to interpret trends in MORB chemistry uniquely given our results (or those of any forward model at this time), our results provide a baseline for understanding how heterogeneity of the source composition can contribute to the range in FeO and Na₂O observed in erupted lavas.

CaO/Al₂O₃

Niu & Hékinian (1997b) have used the CaO/Al₂O₃ ratio in MORB as an indicator of extent of melting and have argued for a global correlation between extent of melting and spreading rate. Hirschmann *et al.* (1999b), however, showed that although CaO/Al₂O₃ increases monotonically with the extent of melting up to the exhaustion of cpx for any given source composition, when comparing isobaric 1 GPa batch melts of different sources, its behavior can be complex and counterintuitive. In particular, as CaO in the melt is strongly influenced by the Na content and by temperature, under isobaric conditions it is higher at equal F in liquids from more depleted sources, even though the source compositions have less CaO. The behavior of Al₂O₃ is more similar to an ordinary incompatible element and is therefore lower in melts from more depleted sources with less Al₂O₃. Hence CaO/Al₂O₃ during progressive isobaric melting is significantly higher at given melt fraction up to the exhaustion of cpx in liquids produced from more depleted sources, and it does not reflect in any simple way the CaO/Al₂O₃ of the source composition. The CaO/Al₂O₃

ratios of the five sources used in the present calculations are all between 0.78 and 0.82; this variation is not a significant contributor to the large variations in liquid $\text{CaO}/\text{Al}_2\text{O}_3$ that result from source heterogeneity.

The variation in $\text{CaO}/\text{Al}_2\text{O}_3$ with source enrichment at equal F that was noted by Hirschmann *et al.* (1999b) for isobaric 1 GPa melts is also seen for polybaric fractional melts at $T_p = 1325^\circ\text{C}$ in incremental liquids at any P where cpx remains in the residue (Fig. 13a) and in active (Fig. 13b) or passive-flow (Fig. 13c) aggregate liquids at any P_f or T_p , whether cpx-out is encountered or not. For a constant F_{max} of 0.1 for the passive flow, fractional fusion case shown in Fig. 13c, a range of $\text{CaO}/\text{Al}_2\text{O}_3$ from 0.35 to 0.85 is produced by a range of 20% enrichment or depletion in a basaltic component in the source (associated with a range of only 0.78–0.82 in $\text{CaO}/\text{Al}_2\text{O}_3$ of the sources). Similarly, a $\text{CaO}/\text{Al}_2\text{O}_3$ of 0.6 is consistent with F_{max} ranging from 0.02 to 0.25 for this same range of source compositions. It should be noted that the low-degree liquids from the fertile sources are much richer in Na than the basaltic component used to generate the source enrichment vector; hence the $\text{CaO}/\text{Al}_2\text{O}_3$ in incremental fractional liquids from the enriched sources rises to the solidus value for the depleted sources after a mass extracted much smaller (about one-quarter) than the difference in mass of basaltic component between the sources (Fig. 13a).

The systematics of $\text{CaO}/\text{Al}_2\text{O}_3$ described above for variable P_f at a potential temperature of 1325°C is also observed in integrated liquids observed at $P_f = P_c$ from melting at other potential temperatures. The essential point is that $\text{CaO}/\text{Al}_2\text{O}_3$ is sensitive to both extent of melting and source composition. As observed for the variable- P_f systematics, a constant F_{max} can yield a large range of $\text{CaO}/\text{Al}_2\text{O}_3$, and a $\text{CaO}/\text{Al}_2\text{O}_3$ of, for example, 0.6 is consistent with F_{max} ranging from 0.04 (for a depleted source) to 0.2 (for an enriched source) for passive flow, fractional fusion (Fig. 13e), despite the fact that the sources display such a small range in this ratio.

This analysis of integrated liquid compositions from heterogeneous sources does not support the contention of Niu & Hékinian (1997b) that $\text{CaO}/\text{Al}_2\text{O}_3$ (or Ca_8/Al_8) would be a more reliable indicator of extent of melting in oceanic basalts than Na_8 . Given that CaO and Al_2O_3 as major oxides are typically less variable in source compositions than incompatible minor elements, Niu & Hékinian plausibly assumed that $\text{CaO}/\text{Al}_2\text{O}_3$ in erupted liquids is less likely than Na_2O content (or other incompatible or trace elements) to be confounded by source heterogeneity. Our calculations [as well as experiments reviewed by Hirschmann *et al.* (1999b)] show instead that the influence of plausible variations in source composition on phase equilibria [in particular, as emphasized by Hirschmann *et al.* (1999b), the influence of Na content on the activity coefficient of CaO in silicate melts] is

sufficient to lead to large variations in $\text{CaO}/\text{Al}_2\text{O}_3$, such that this ratio, when considered on its own, is unlikely to offer any improvement over Na_8 as a direct indicator of degree of melting. Our results also show that this ratio is not a straightforward indicator of the total mass of liquid that has been extracted relative to a reference source, as the alkali content of liquids is an important factor and this is not a simple function of total extent of melting. Tests to deconvolve the effects of source heterogeneity from extent of melting are instead likely to require consideration of multiple chemical and isotopic indicators (see Hirschmann *et al.*, 1999b).

FeO* and $\text{K}_2\text{O}/\text{TiO}_2$

Hirschmann *et al.* (1999b) showed that at any given MgO content isobaric 1 GPa batch melts produced from depleted (i.e. high *mg*-number) sources are lower in FeO* than liquids produced from enriched (low *mg*-number) sources. Hence, they argued, the negative correlation between $\text{K}_2\text{O}/\text{TiO}_2$ (often considered a reliable and increasing function of source enrichment, similar to normalized La/Sm; see Schilling, 1975) and Fe_8 in regionally averaged basalts observed by Shen & Forsyth (1995), reproduced here in Fig. 15 (see below), is unlikely to be due to typical mantle heterogeneity. This calls into question the attempt by Shen & Forsyth to eliminate the effects of heterogeneity on the MORB global trend by using the trend shown in Fig. 15 to correct Fe_8 to a constant $\text{K}_2\text{O}/\text{TiO}_2$. As source variation of the type considered by Hirschmann *et al.* (1999b) would be expected to produce positive correlations in Fig. 15, the observed trend must reflect other factors or a type of source heterogeneity different from that characterizing oceanic and alpine peridotite suites. In this section, we extend the isobaric trends examined by Hirschmann *et al.* (1999b) to polybaric melting regimes.

The conclusion from isobaric considerations generalizes to integrated polybaric melt compositions: at a given MgO content, partial melts of relatively enriched source peridotites have higher FeO contents. Whether examined for either active or passive flow across the full range of potential temperature from 1200 to 1600°C , we see that FeO* increases with source enrichment whether viewed at equal P_f (Fig. 14b and c), equal T_p (Fig. 14d and e), or equal MgO (Fig. 14b–e). Hence, we conclude that integrated melt compositions of sources enriched in a basalt component, regardless of the details of the integrations, will produce liquids with higher FeO* contents than liquids from depleted sources. A similar result was shown for one potential temperature by Langmuir *et al.* (1992, fig. 58). These FeO* differences in primary liquids will, following Langmuir & Hanson (1980), be largely preserved in fractionated melts. As the

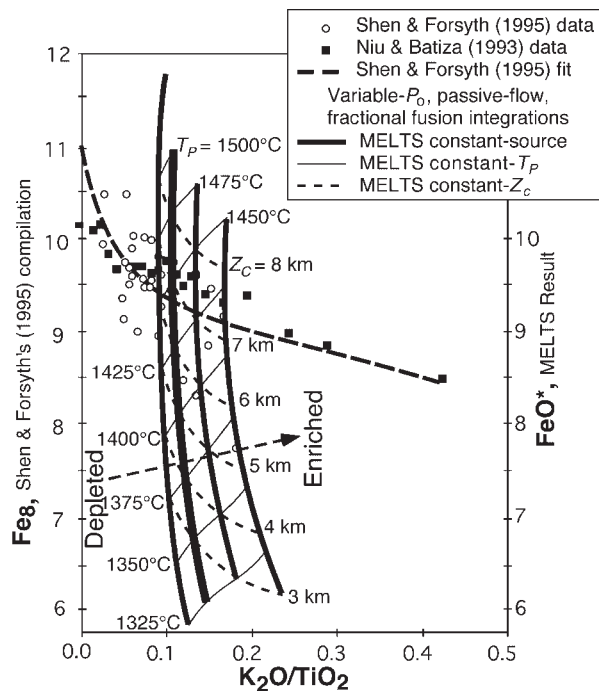


Fig. 15. Fe_8 vs K_2O/TiO_2 for regionally averaged MORB compositions from Shen & Forsyth (1995). (○, Shen & Forsyth's compilation of normal ridges; ■, data of Niu & Batiza (1993) including hotspot-affected regions. The heavy dashed curve is a fit to the average MORBs by Shen & Forsyth.) The MORB data are compared with FeO^* vs K_2O/TiO_2 for primary aggregate liquids predicted by MELTS from passive flow, fractional melting, variable- P_0 melting regimes for four source compositions. Bold curves show equal source composition as T_P is varied [Cr-bearing Hart & Zindler (1986) reference composition extrapolated]; light curves with positive slope show the effect of heterogeneity at constant potential temperature; light dashed curves with negative slope show heterogeneity at constant crustal thickness. The most depleted composition shown in Figs 10–14 is not shown for reasons of clarity; it cuts across the grid defined by the other four compositions.

melts of enriched sources will also have higher K_2O/TiO_2 (see below), we concur with the conclusion of Hirschmann *et al.* (1999b) based on simpler isobaric calculations that the Shen & Forsyth (1995) observation of a negative correlation between Fe_8 and K_2O/TiO_2 is unlikely to reflect source heterogeneity of the type considered here, namely addition or subtraction of a broadly basaltic component.

Although we generally exclude K_2O from our modeling, Fig. 15 shows the result of variable- P_0 , passive-flow, fractional melting calculations in which we have treated K_2O as a simple trace component with a constant bulk D of 0.01. TiO_2 and FeO^* contents are based on the full thermodynamic MELTS calculation. As discussed above, it is difficult at present to fractionate MELTS output liquids to 8% MgO, but primary liquids with MgO >8% should not change significantly in FeO^* or K_2O/TiO_2 when fractionated to 8% MgO at low pressure (Langmuir & Hanson, 1980; Grove *et al.*, 1992; Langmuir

et al., 1992), so MELTS results expressed as primary FeO^* are plotted together with the Niu & Batiza (1993) and Shen & Forsyth (1995) compilations of Fe_8 averages. The K_2O contents of natural peridotites are extremely scattered and define no clear trend against MgO or mg -number (Fig. 10). For this calculation, as we consider K to be more incompatible than Ti, we choose K_2O in the mixed sources such that the K_2O/TiO_2 ratio of the source increases linearly with enrichment in other fertile components (0.06 for the composition depleted by 10% basalt extraction, 0.18 for the Hart & Zindler primitive upper mantle, 0.30 for the composition enriched by 10% basalt addition; see Fig. 10). As shown in Fig. 15, for typical oceanic potential temperatures (1325–1500°C are shown) and crustal thickness, the MELTS calculations of variable- P_0 passive, fractional melting regimes with $P_f = P_c$ yield a small range (~ 0.05) of K_2O/TiO_2 values in integrated primary melt compositions for each given source composition (i.e. the heavy curves in Fig. 15 are nearly vertical), although a larger range results if the calculations are extended to even lower T_P . The calculated range in K_2O/TiO_2 for each fixed source composition is similar to the calculation of Shen & Forsyth (1995), although those workers used constant partition coefficients for both K and Ti and variable- P_f systematics (as opposed to the variable- P_0 model used here). Although the most depleted composition is not shown in Fig. 15 because its curve crosses the others (i.e. giving higher K_2O/TiO_2 at equal FeO^* than the next most depleted composition), these curves demonstrate the important point that, if all melts produced in the mantle are integrated to produce the crust and there is a reasonable amount of K_2O in the source composition, there is no way for our models to produce average crust (i.e. integrated melt compositions) with K_2O/TiO_2 ratios as low as the lowest regionally averaged MORB compositions plotted in Fig. 15. Successful models will need to consider the effect of removing some low-melt fraction increments of liquid from the aggregate primary melt, perhaps by dynamical effects that lead to imperfect focusing and mixing of melts at the axis (e.g. Spiegelman, 1996).

Variations in the source composition at equal potential temperature, as anticipated above, yield according to MELTS positive slopes in FeO vs K_2O/TiO_2 (these trends are shown by the light continuous curves in Fig. 15) rather than the overall negative trend of the MORB data. This indicates, as argued above, that the negative correlation between Fe_8 and K_2O/TiO_2 emphasized by Shen & Forsyth is not due to heterogeneity of the type tested (and at constant potential temperature using passive flow and fractional fusion) and that correction of Fe_8 to constant K_2O/TiO_2 as a step in testing a constant- T_P model of global variation is unjustified. On the other hand, in Fig. 15 we also show (as short-dashed curves) contours of equal crustal thickness across four source

compositions (passive flow, fractional fusion). More enriched sources require lower T_p to generate the same amount of crust as more depleted sources, so these contours are rotated with respect to the constant- T_p contours. We thus find that source variations of the type tested do generate negative correlations between FeO^* and $\text{K}_2\text{O}/\text{TiO}_2$ at constant crustal thickness with, generally speaking, the same sense of curvature as the observed regional averages, but with insufficient total ranges in $\text{K}_2\text{O}/\text{TiO}_2$ to explain the MORB data. It would require, however, a fortuitous relationship between source composition and potential temperature to generate these equal- ζ_c trends. Indeed, if any relationship between source composition and potential temperature did exist, one might expect instead that enriched regions, associated with hotspots, would have higher-than-average potential temperature, resulting in positively sloped trends even steeper than the equal- T_p contours in Fig. 15.

Although the negative correlation between FeO^* and $\text{K}_2\text{O}/\text{TiO}_2$ cannot be simply explained by regional-scale variations in source composition along a bulk basaltic enrichment–depletion trend, it remains a robust observation. In fact, similar relationships are found in regional datasets, e.g. near the Galapagos (Fisk *et al.*, 1982) and the Azores (Asimow & Langmuir, 1998) hotspots. The origin of this low-Fe signal in enriched MORB remains an important but unanswered question. The solution may require consideration of enrichment by very small degree melts and/or the effects of water on melting and fractionation of melts from enriched sources.

CONCLUSIONS

This paper presents the results of modeling the production of MORB by melting of upwelling peridotite using the current calibration of the MELTS software. Some conclusions are necessarily provisional because the model is imperfect, and it can be difficult to distinguish robust predictions from artifacts. We have confidence that the model itself will continue to improve as users of the model identify its shortcomings and point the way to critical experiments for improving the calibration. The key results of our calculations are as follows:

(1) the effects of the spinel–plagioclase peridotite transition on the volume of basalt produced by adiabatic decompression become increasingly important for potential temperatures $\leq 1280^\circ\text{C}$. The extreme depression of the solidus and negative slope through the region 0.5–1.0 GPa predicted by MELTS is testable provided that very low melt fractions ($<1\%$) can be recognized experimentally.

(2) The predicted presence of a maximum potential temperature along the solidus in the upper mantle is also subject to experimental verification, but this will require

data on thermal expansivity of solids at high pressure as well as phase equilibrium experiments.

(3) The variable productivity and curved solidus predicted by MELTS translate into nonlinear relations between the potential temperature and initial pressure of melting, as well as nonlinear relations among the pressure interval of melting and the mean pressure of melting, mean extent of melting, and crustal thickness. Crustal thickness is the most easily measured of these variables, but as some cannot be directly measured at all, these predicted relations are not easily testable. However, the relationships of these variables to melt chemistry can be predicted subject to assumptions about melt generation and transport, so progress in interpreting melt compositions or perhaps consideration of residual peridotite compositions could translate into constraints on melting conditions and processes. An important prediction of MELTS, however, is that crustal thicknesses above ~ 13 – 15 km (e.g. near hotspots) require mechanisms other than pure incrementally adiabatic fractional melting accompanying passive flow.

(4) The novel productivity behavior of MELTS leads, in conjunction with the model incremental liquids, to quantitative, internally consistent predictions of trends in melt compositions as functions of initial and final pressures of melting and source composition. The current MELTS calibration does not reproduce the global Na_2O – FeO^* trend of fractionation-corrected, regionally averaged MORB compositions (Klein & Langmuir, 1987). Although this reflects in detail the inaccurate predictions of Na partitioning by MELTS and the necessity of extrapolating to melting regimes that extend deeper than the calibrated range of MELTS, the lowest Na_8 ridge segments are inconsistent with passive-flow mixing for any chemical model when productivity variations are accounted for, suggesting either a component of active flow or source heterogeneity.

(5) MELTS calculations suggest that local trends in basalt compositions at slow-spreading ridges, i.e. correlations with low positive slope between Na_8 and Fe_8 of individual samples from a ridge segment (Klein & Langmuir, 1989) cannot be fully explained by source heterogeneity, extraction of unmixed increments of liquid from within a melting regime, or partial mixtures from any simple melting regime of the types modeled so far.

(6) The standard mixing models describing end-member active and passive flow appear to be oversimplified compared with what will be required for detailed evaluation of many aspects of mid-ocean ridge processes. Dynamically based calculations of actual melt transport and mixing paths may be necessary for models of mantle melting to be capable of describing the details of actual MORB chemistry.

(7) $\text{CaO}/\text{Al}_2\text{O}_3$ in aggregate melts is sensitive to source compositions; i.e. $\text{CaO}/\text{Al}_2\text{O}_3$ ratios of melts of depleted

sources are systematically higher than those of enriched sources at the same degree of melting. A reasonable range of heterogeneity in the source can confound the simple dependence on melt fraction seen for an individual source composition. Consequently, it is problematic to use $\text{CaO}/\text{Al}_2\text{O}_3$ in observed lavas as a direct constraint on extent of partial melting.

(8) It is unlikely that the well-defined negative $\text{K}_2\text{O}/\text{TiO}_2$ vs FeO^* correlation observed for regional averages of MORBs is controlled by source heterogeneity in the sense of bulk addition or depletion of basalt to the source. Instead, $\text{K}_2\text{O}/\text{TiO}_2$ and FeO^* correlate positively in MELTS-calculated aggregate primary melts as the result of source variations of this type.

ACKNOWLEDGEMENTS

The authors gratefully acknowledge constructive reviews by Emily Klein, Jennifer Witter, and Kevin Johnson, and especially heroic editorial handling by Dennis Geist. P.D.A. was supported during part of this work by a postdoctoral research fellowship from Lamont–Doherty Earth Observatory. This work was supported by NSF grants OCE-9711735 to M.M.H., and EAR-9219899, OCE-9504517 and EAR-9706254 to E.M.S.

REFERENCES

- Asimow, P. D. (1997). A thermodynamic model of adiabatic melting of the mantle. Ph.D. thesis, California Institute of Technology, Pasadena.
- Asimow, P. D. & Langmuir, C. H. (1998). Segment-scale and regional systematics from 33°N to 41°N on the Mid-Atlantic Ridge: results from the FAZAR Cruise. *EOS Transactions, American Geophysical Union* **79**, F938–F939.
- Asimow, P. D. & Stolper, E. M. (1999). Steady-state mantle–melt interactions in one dimension: 1. Equilibrium transport and melt focusing. *Journal of Petrology* **40**, 475–494.
- Asimow, P. D., Hirschmann, M. M., Ghiorso, M. S., O'Hara, M. J. & Stolper, E. M. (1995). The effect of pressure-induced solid–solid phase transitions on decompression melting of the mantle. *Geochimica et Cosmochimica Acta* **59**, 4489–4506.
- Asimow, P. D., Hirschmann, M. M. & Stolper, E. M. (1997). An analysis of variations in isentropic melt productivity. *Philosophical Transactions of the Royal Society of London, Series A* **355**, 255–281.
- Baker, M. B. & Stolper, E. M. (1994). Determining the composition of high-pressure mantle melts using diamond aggregates. *Geochimica et Cosmochimica Acta* **58**, 2811–2827.
- Baker, M. B., Hirschmann, M. M., Ghiorso, M. S. & Stolper, E. M. (1995). Compositions of low-degree partial melts of peridotite: results from experiments and thermodynamic calculations. *Nature* **375**, 308–311.
- Batchelor, G. K. (1967). *An Introduction to Fluid Dynamics*. Cambridge: Cambridge University Press.
- Brodholt, J. P. & Batiza, R. (1989). Global systematics of unaveraged mid-ocean ridge basalt compositions: Comment on 'Global correlations of ocean ridge basalt chemistry with axial depth and crustal thickness'. *Journal of Geophysical Research* **94**, 4231–4239.
- Coulton, A. J., Harper, G. D. & Ohanley, D. S. (1995). Oceanic versus emplacement age serpentinization in the Josephine Ophiolite—implications for the nature of the Moho at intermediate and slow-spreading ridges. *Journal of Geophysical Research* **100**, 22245–22260.
- Dick, H. J. B., Fisher, R. L. & Bryan, W. B. (1984). Mineralogic variability of the uppermost mantle along mid-ocean ridges. *Earth and Planetary Science Letters* **69**, 88–106.
- Fisk, M. R., Bence, A. E. & Schilling, J.-G. (1982). Major element chemistry of Galapagos Rift Zone magmas and their phenocrysts. *Earth and Planetary Science Letters* **61**, 171–189.
- Forsyth, D. W. (1992). Geophysical constraints on mantle flow and melt generation beneath mid-ocean ridges. In: Phipps Morgan, J., Blackman, D. K. & Sinton, J. M. (eds) *Mantle Flow and Melt Generation at Mid-Ocean Ridges*. *Geophysical Monograph, American Geophysical Union* **71**, 1–66.
- Frey, F. A., Suen, C. J. & Stockman, H. W. (1985). The Ronda high-temperature peridotite: geochemistry and petrogenesis. *Geochimica et Cosmochimica Acta* **49**, 2469–2491.
- Ghiorso, M. S. (1994). Algorithms for the estimation of phase stability in heterogeneous thermodynamic systems. *Geochimica et Cosmochimica Acta* **58**, 5489–5501.
- Ghiorso, M. S. & Sack, R. O. (1995). Chemical mass transfer in magmatic processes IV. A revised and internally consistent thermodynamic model for the interpolation and extrapolation of liquid–solid equilibria in magmatic systems at elevated temperatures and pressures. *Contributions to Mineralogy and Petrology* **119**, 197–212.
- Green, D. H. (1973). Experimental studies on a model upper mantle composition at high pressure under water-saturated and water-undersaturated conditions. *Earth and Planetary Science Letters* **19**, 37–53.
- Grove, T. L., Kinzler, R. J. & Bryan, W. B. (1992). Fractionation of mid-ocean ridge basalt (MORB). In: Phipps Morgan, J., Blackman, D. K. & Sinton, J. M. (eds) *Mantle Flow and Melt Generation at Mid-Ocean Ridges*. *Geophysical Monograph, American Geophysical Union* **71**, 281–310.
- Hart, S. R. & Zindler, A. (1986). In search of a bulk-earth composition. *Chemical Geology* **57**, 247–267.
- Herzberg, C., Feigenson, M., Skuba, C. & Ohtani, E. (1988). Majorite fractionation recorded in the geochemistry of peridotites from South Africa. *Nature* **332**, 823–826.
- Hirose, K. & Kushiro, I. (1998). The effect of melt segregation on polybaric mantle melting: estimation from the incremental melting experiments. *Physics of the Earth and Planetary Interiors* **107**, 111–118.
- Hirschmann, M. M. & Stolper, E. M. (1996). A possible role for garnet pyroxenite in the origin of the 'garnet signature' in MORB. *Contributions to Mineralogy and Petrology* **124**, 185–208.
- Hirschmann, M. M., Stolper, E. M. & Ghiorso, M. S. (1994). Perspectives on shallow mantle melting from thermodynamic calculations. *Mineralogical Magazine* **58A**, 418–419.
- Hirschmann, M. M., Baker, M. B. & Stolper, E. M. (1998a). The effect of alkalis on the silica content of mantle-derived melts. *Geochimica et Cosmochimica Acta* **62**, 883–902.
- Hirschmann, M. M., Ghiorso, M. S., Waslylenki, L. E., Asimow, P. D. & Stolper, E. M. (1998b). Calculation of peridotite partial melting from thermodynamic models of minerals and melts. I. Review of methods and comparison to experiments. *Journal of Petrology* **39**, 1091–1115.
- Hirschmann, M. M., Asimow, P. D., Ghiorso, M. S. & Stolper, E. M. (1999a). Calculation of peridotite partial melting from thermodynamic models of minerals and melts. III. Controls on isobaric melt production and the effect of water on melt production. *Journal of Petrology* **40**, 831–851.
- Hirschmann, M. M., Ghiorso, M. S. & Stolper, E. M. (1999b). Calculation of peridotite partial melting from thermodynamic models

- of minerals and melts. II. Isobaric variations in melts near the solidus and owing to variable source composition. *Journal of Petrology* **40**, 297–313.
- Hirth, G. & Kohlstedt, D. L. (1996). Water in the oceanic upper mantle: implications for rheology, melt extraction and the evolution of the lithosphere. *Earth and Planetary Science Letters* **144**, 93–108.
- Humler, E., Thiroit, J. L. & Montagner, J. P. (1993). Global correlations of mid-ocean-ridge basalt chemistry with seismic tomographic images. *Nature* **364**, 225–228.
- Ito, G., Shen, Y., Hirth, G. & Wolfe, C. J. (1999). Mantle flow, melting, and dehydration of the Iceland mantle plume. *Earth and Planetary Science Letters* **165**, 81–96.
- Iwamori, H., McKenzie, D. P. & Takahashi, E. (1995). Melt generation by isentropic mantle upwelling. *Earth and Planetary Science Letters* **134**, 253–266.
- Johnson, K. T. M. & Dick, H. J. B. (1992). Open system melting and temporal and spatial variation of peridotite and basalt at the Atlantis II Fracture Zone. *Journal of Geophysical Research* **97**, 9219–9241.
- Johnson, K. T. M., Dick, H. J. B. & Shimizu, N. (1990). Melting in the oceanic upper mantle: an ion microprobe study of diopsides in abyssal peridotites. *Journal of Geophysical Research* **95**, 2661–2678.
- Karato, S. I. & Jung, H. (1998). Water, partial melting and the origin of the seismic low velocity and high attenuation zone in the upper mantle. *Earth and Planetary Science Letters* **157**, 193–207.
- Kelemen, P. B., Hirth, G., Shimizu, N., Spiegelman, M. & Dick, H. J. B. (1997). A review of melt migration processes in the adiabatically upwelling mantle beneath oceanic spreading ridges. *Philosophical Transactions of the Royal Society of London, Series A* **355**, 283–318.
- Kinzler, R. J. (1997). Melting of mantle peridotite at pressures approaching the spinel to garnet transition: application to mid-ocean ridge basalt petrogenesis. *Journal of Geophysical Research* **102**, 853–874.
- Kinzler, R. J. & Grove, T. L. (1992a). Primary magmas of mid-ocean ridge basalts 1. Experiments and methods. *Journal of Geophysical Research* **97**, 6885–6906.
- Kinzler, R. J. & Grove, T. L. (1992b). Primary magmas of mid-ocean ridge basalts 2. Applications. *Journal of Geophysical Research* **97**, 6907–6926.
- Klein, E. M. & Langmuir, C. H. (1987). Global correlations of ocean ridge basalt chemistry with axial depth and crustal thickness. *Journal of Geophysical Research* **92**, 8089–8115.
- Klein, E. M. & Langmuir, C. H. (1989). Local versus global variations in ocean ridge basalt composition: a reply. *Journal of Geophysical Research* **94**, 4241–4252.
- Korenaga, J., Hollbrook, W. S., Kent, G. M., Kelemen, P. B., Detrick, R. S., Larsen, H. C., Hopper, J. R. & Dahl-Jensen, T. (2000). Crustal structure of the southeast Greenland margin from joint refraction and reflection seismic tomography. *Journal of Geophysical Research* **105**, 21591–21614.
- Kushiro, I. (1996). Partial melting of a fertile mantle peridotite at high pressure: and experimental study using aggregates of diamond. In: Basu, A. & Hart, S. (eds) *Earth Processes: Reading the Isotopic Clock. Geophysical Monograph, American Geophysical Union* **95**, 109–122.
- Langmuir, C. H. & Hanson, G. N. (1980). An evaluation of major element heterogeneity in the mantle sources of basalts. *Philosophical Transactions of the Royal Society of London, Series A* **297**, 383–407.
- Langmuir, C. H., Klein, E. M. & Plank, T. (1992). Petrological systematics of mid-ocean ridge basalts: constraints on melt generation beneath ocean ridges. In: Phipps Morgan, J., Blackman, D. K. & Sinton, J. M. (eds) *Mantle Flow and Melt Generation at Mid-Ocean Ridges. Geophysical Monograph, American Geophysical Union* **71**, 183–280.
- McKenzie, D. P. (1984). The generation and compaction of partial melts. *Journal of Petrology* **25**, 713–765.
- McKenzie, D. P. & Bickle, M. J. (1988). The volume and composition of melt generated by extension of the lithosphere. *Journal of Petrology* **29**, 625–679.
- McKenzie, D. P. & O’Nions, R. K. (1991). Partial melt distributions from inversion of rare earth element concentrations. *Journal of Petrology* **32**, 1021–1091.
- MELT Seismic Team (1998). Imaging the deep seismic structure beneath a mid-ocean ridge: The MELT experiment. *Science* **280**, 1215–1218.
- Menke, W. (1999). Crustal isostasy indicates anomalous densities beneath Iceland. *Geophysical Research Letters* **26**, 1215–1218.
- Muller, M. R., Robinson, C. J., Minshull, T. A., White, R. S. & Bickle, M. J. (1997). Thin crust beneath ocean drilling program borehole 735B at the Southwest Indian Ridge? *Earth and Planetary Science Letters* **148**, 93–107.
- Niu, Y. & Batiza, R. (1991). An empirical method for calculating melt compositions produced beneath mid-ocean ridges: application to axis and off-axis (seamounts) melting. *Journal of Geophysical Research* **96**, 21753–21777.
- Niu, Y. & Batiza, R. (1993). Chemical variation trends at fast and slow spreading mid-ocean ridges. *Journal of Geophysical Research* **98**, 7887–7902.
- Niu, Y. & Hékinian, R. (1997a). Basaltic liquids and harzburgitic residues in the Garrett Transform—a case study at fast-spreading ridges. *Earth and Planetary Science Letters* **146**, 243–258.
- Niu, Y. & Hékinian, R. (1997b). Spreading-rate dependence of the extent of melting beneath ocean ridges. *Nature* **385**, 326–329.
- Niu, Y. L., Waggoner, D. G., Sinton, J. M. & Mahoney, J. J. (1996). Mantle source heterogeneity and melting processes beneath seafloor spreading centers: the East Pacific Rise, 18°S–19°S. *Journal of Geophysical Research* **101**, 27711–27733.
- O’Hara, M. J. (1968). Are ocean floor basalts primary magmas? *Nature* **220**, 683–686.
- Plank, T. & Langmuir, C. H. (1992). Effects of the melting regime on the composition of oceanic crust. *Journal of Geophysical Research* **97**, 19749–19770.
- Plank, T., Spiegelman, M., Langmuir, C. H. & Forsyth, D. W. (1995). The meaning of ‘mean F’: clarifying the mean extent of melting at ocean ridges. *Journal of Geophysical Research* **100**, 15045–15052.
- Presnall, D. C. (1969). The geometrical analysis of partial fusion. *American Journal of Science* **267**, 1178–1194.
- Presnall, D. C., Dixon, J. R., O’Donnell, T. H. & Dixon, S. A. (1979). Generation of mid-ocean ridge tholeiites. *Journal of Petrology* **20**, 3–35.
- Reynolds, J. R. (1995). Segment-scale systematics of mid-ocean ridge magmatism and geochemistry. Ph.D. thesis, Columbia University, New York.
- Richardson, C. & McKenzie, D. (1994). Radioactive disequilibria from 2D models of melt generation by plumes and ridges. *Earth and Planetary Science Letters* **128**, 425–437.
- Salter, V. J. M. (1996). The generation of mid-ocean ridge basalts from the Hf and Nd isotope perspective. *Earth and Planetary Science Letters* **141**, 109–123.
- Schilling, J.-G. (1975). Rare-earth variations across ‘normal segments’ of the Reykjanes Ridge, 60°–53°N, Mid-Atlantic Ridge, 29°S, and East Pacific Rise, 2°S–19°S, and evidence on the composition of the underlying low-velocity layer. *Journal of Geophysical Research* **80**, 1459.
- Scott, D. R. & Stevenson, D. J. (1989). A self-consistent model of melting, magma migration and buoyancy-driven circulation beneath mid-ocean ridges. *Journal of Geophysical Research* **94**, 2973–2988.

- Shen, Y. & Forsyth, D. W. (1992). The effects of temperature- and pressure-dependent viscosity on three-dimensional passive flow of the mantle beneath a ridge–transform system. *Journal of Geophysical Research* **97**, 19717–19728.
- Shen, Y. & Forsyth, D. W. (1995). Geochemical constraints on initial and final depths of melting beneath mid-ocean ridges. *Journal of Geophysical Research* **100**, 2211–2237.
- Spiegelman, M. (1996). Geochemical consequences of melt transport in 2-D: the sensitivity of trace elements to mantle dynamics. *Earth and Planetary Science Letters* **139**, 115–132.
- Spiegelman, M. & McKenzie, D. (1987). Simple 2-D models for melt extraction at mid-ocean ridges and island arcs. *Earth and Planetary Science Letters* **83**, 137–152.
- Takahashi, E. (1986). Melting of a dry peridotite KLB-1 up to 14 GPa: implications on the origin of peridotitic upper mantle. *Journal of Geophysical Research* **91**, 9367–9380.
- Takahashi, E., Shimazaki, T., Tsuzaki, Y. & Yoshida, H. (1993). Melting study of a peridotite KLB-1 to 6.5 GPa, and the origin of basaltic magmas. *Philosophical Transactions of the Royal Society of London, Series A* **342**, 105–120.
- Verhoogen, J. (1965). Phase changes and convection in the Earth's mantle. *Philosophical Transactions of the Royal Society of London, Series A* **258**, 276–283.
- von Bagen, N. & Waff, H. S. (1986). Permeabilities, interfacial areas and curvatures of partially molten systems: results of numerical computations of equilibrium microstructures. *Journal of Geophysical Research* **91**, 9261–9276.
- Walker, D., Agee, C. B. & Zhang, Y. (1988). Fusion curve slope and crystal/liquid buoyancy. *Journal of Geophysical Research* **93**, 313–323.
- Wasylenki, L. E., Baker, M. B., Hirschmann, M. M. & Stolper, E. M. (1996). The effect of source depletion on equilibrium mantle melting. *EOS Transactions, American Geophysical Union* **77**, F847.
- Watson, S. & McKenzie, D. P. (1991). Melt generation by plumes: a study of Hawaiian volcanism. *Journal of Petrology* **32**, 501–537.
- Weaver, J. & Langmuir, C. H. (1990). Calculation of phase equilibrium in mineral–melt systems. *Computers and Geosciences* **16**, 1–19.
- Wolfe, C. J., Bjarnason, I. T., Solomon, S. C. & VanDecar, J. C. (1996). Three-dimensional seismic imaging of the Icelandic hot spot: results from the ICEMELT experiment. *American Geophysical Union 1996 Spring Meeting, EOS Transactions, American Geophysical Union* **77**, 276.
- Wyllie, P. J. & Wolf, M. B. (1993). Amphibole dehydration–melting: sorting out the solidus. In: Prichard, H. M., Alabaster, T., Harris, N. B. W. & Neary, C. R. (eds) *Magmatic Processes and Plate Tectonics*. Geological Society, London, *Special Publications* **76**, 405–416.
- Zhang, J. & Herzberg, C. (1994). Melting experiments on anhydrous peridotite KLB-1 from 5.0 to 22.5 GPa. *Journal of Geophysical Research* **99**, 17729–17742.
- Zhang, Y. S., Tanimoto, T. & Stolper, E. M. (1994). S-wave velocity, basalt chemistry and bathymetry along the Mid-Atlantic Ridge. *Physics of the Earth and Planetary Interiors* **84**, 79–93.
- Zindler, A., Salters, V. J. M., Bourdon, B. & Elliot, T. E. (1996). Plumes and plums in the MORB mantle. *Journal of Conference Abstracts* **1**, 700.